Modeling of Copper Migration In CdTe Photovoltaic Devices

by

Da Guo

A Dissertation Presented in Partial Fulfillment
of the Requirements for the Degree
Doctor of Philosophy

Approved October 2017 by the
Graduate Supervisory Committee:

Dragica Vasileska, Chair
Mariana Bertoni
Igor Sankin
Stephen Goodnick

ARIZONA STATE UNIVERSITY

December 2017

ABSTRACT

Thin-film modules of all technologies often suffer from performance degradation over time. Some of the performance changes are reversible and some are not, which makes deployment, testing, and energy-yield prediction more challenging. The most commonly alleged causes of instability in CdTe device, such as "migration of Cu," have been investigated rigorously over the past fifteen years. As all defects, intrinsic or extrinsic, interact with the electrical potential and free carriers so that charged defects may drift in the electric field and changing ionization state with excess free carriers. Such complexity of interactions in CdTe makes understanding of temporal changes in device performance even more challenging. The goal of the work in this dissertation is, thus, to eliminate the ambiguity between the observed performance changes under stress and their physical root cause by enabling a depth of modeling that takes account of diffusion and drift at the atomistic level coupled to the electronic subsystem responsible for a PV device's function. The 1D Unified Solver, developed as part of this effort, enables us to analyze PV devices at a greater depth.

In this dissertation, the implementation of a drift-diffusion model defect migration simulator, development of an implicit reaction scheme for total mass conservation, and a couple of other numerical schemes to improve the overall flexibility and robustness of this coupled Unified Solver is discussed. Preliminary results on Cu (with or without Cl-treatment) annealing simulations in both single-crystal CdTe wafer and poly-crystalline CdTe devices show promising agreement to experimental findings, providing a new perspective in the research of improving doping concentration hence the open-circuit voltage of CdTe technology. Furthermore, on the reliability side, in agreement of previous

experimental reports, simulation results suggest possibility of Cu depletion in short-circuited cells stressed at elevated temperature. The developed solver also successfully demonstrated that mobile donor migration can be used to explain solar cell performance changes under different stress conditions.

DEDICATION

Dedicated to Dad, Mom and Meng.

ACKNOWLEDGMENTS

First and foremost, I would like to express my most sincere gratitude to my research advisor Dr. Dragica Vasileska, for her guidance and supervision for the past several years. I have benefited significantly from her clear and deep understanding of semiconductor device physics and numerical simulations. I am deeply grateful to her for recruiting me into her research group and opening a window to scientific research for me. I could not have imagined having another advisor and mentor for my Ph.D study.

I would also like to thank Dr. Igor Sankin, who has truly been a mentor to me, particularly in regards to detailed knowledge of CdTe thin-film photovoltaic devices and tireless instructions related to this research. I am also thankful to Dr. Stephen Goodnick, who generously provided me unlimited access to the Ocotillo cluster for countless simulations in this work. I would also like to thank Dr. Mariana Bertoni, for her wonderful instruction and discussion on semiconductor defects at the early stage of this research. The advice and feedback provided by these committee members are undeniably valuable to this work and I am grateful for that.

I must express my gratitude to many current and previous colleagues for their help and mentoring in the past years. I had a great time with my group mates, especially Yi Fang and Pradyumna Muralidharan, with whom I spent quite some time together after work and in conferences. I would also like to thank people that are directly involved in the PREDICTs and PVRD projects: Dr. Dmitry Krasikov and Dr. Su-Huai Wei provided first principle calculated defect parameters, theoretical models for defect reactions and a lot of helpful discussions, Dr. Christian Ringhofer, Dr. Daniel Brinkman and Dr. Richard Akis were key in the development of the numerical scheme, Dr. Tian Fang and Dr. Andrew

Moore performed all kinds of interesting experiment related to Cu migration and device performance metastabilities in CdTe solar cells. Without either one of them, this work could not be completed.

I am truly grateful to the funding sources that had made this work possible. The research grants that supported this work include: Depart of Energy SunShot Program, Predicts Award DE-EE0006344 and PVRD Award DE-EE0007536 and First Solar Inc., Delphi Projects.

Last but not the least, I must thank my girlfriend, Meng Zhang, and my family, for their love, encouragement and support in all these years.

TABLE OF CONTENTS

Page

CHAPTER Page

LIST OF TABLES

LIST OF FIGURES

CHAPTER 1

INTRODUCTION

The total energy consumption in the US had reached 98.3 quadrillion Btu in 2014, which is a 1 % increase from 2013. A large portion (81 %) of the energy consumption is supplied by fossil fuels, such as petroleum (35 %), natural gas (28 %) and coal (18 %). However, the storage of these fossil fuels is limited on earth and they are considered non-renewable energy sources. As a result, renewable energy (including Biomass, hydropower, solar, wind and geothermal, 10% of the total consumption) usage has seen rapid growth in the last decade. In the US, between the years of 2008 to 2013, the total renewable electricity generation increased by 40 %, and now occupies 14.8 % of the total electricity capacity and 13.1 % of the annual electricity generation.

In particular, Photovoltaic (PV) technology is experiencing the fastest growth among all energy source. In 2014, newly installed PV capacity reached 6.2GW, growing 30% over 2013's total. Solar power accounted for 32 percent of the nation's new generation capacity in 2014, beating both wind energy and coal for the second year in a row. Moreover, PV systems generated 15,874 GWh of power in 2014, almost doubled its 8121 GWh generation in 2013.

Photovoltaic technology is not only experiencing fast growth in market share, but also in technology development. Figure 1.1 below shows the continuous improvements of the best research solar cell efficiencies over the last four decades. Some important accomplishments include: 46 % overall conversion efficiency achieved by concentrated III-V multi-junction solar cells, 25.6 % efficiency achieved by single-crystalline Si solar

cells, 22.3 % efficiency achieved by CIGS solar cell and 22.1 % conversion efficiency achieved by thin-film CdTe technology. Despite the fast growth of PV technology, the percentage of electrical power generated by PV is much smaller than the other energy sources. In 2014, less than 0.5% of the US overall electricity generation was contributed by PV. Even after 2 years of rapid growths, only 1.7% of the US overall electricity was generated by photovoltaic devices, between July 2016 and July 2017.

US Department of Energy launched the SunShot initiative, aiming to make large-scale PV system cost-comparable to other energy sources by 2020, to further increase the market share of Photovoltaics. Among all of the PV technologies, thin-film solar cells show great potential in achieving the goals of improving cell efficiency while further reducing the manufacturing cost. CdTe PV is one of the leading candidates in this competition.

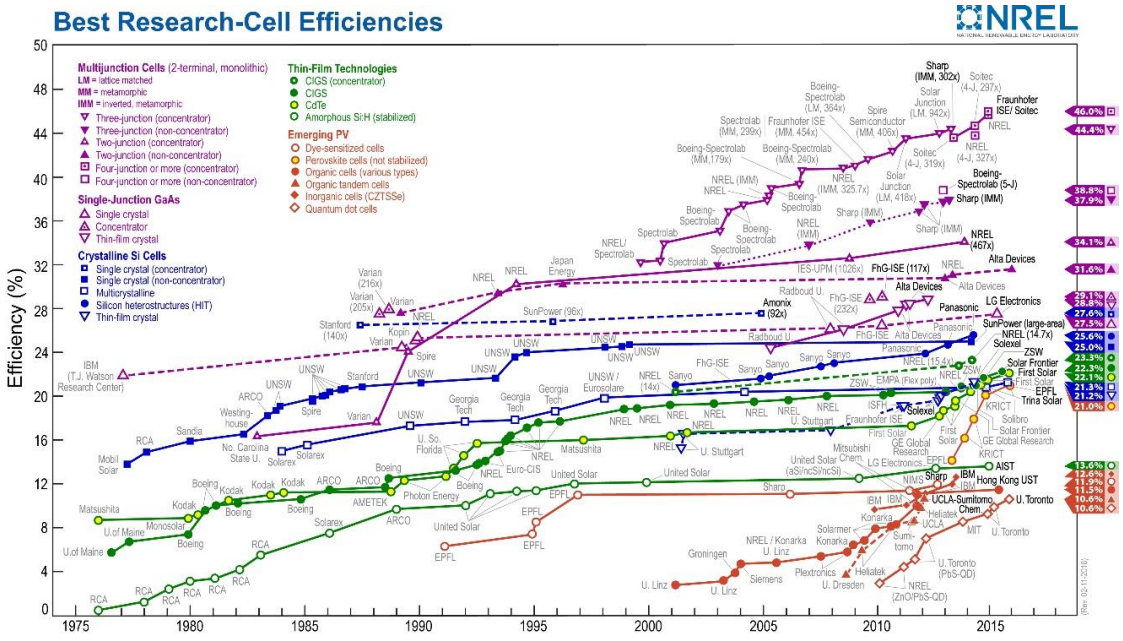

Figure 1.1. Efficiency chart of best research solar cells.

1.1 CdTe PHOTOVOLTAICS

As one of the most successful thin-film photovoltaic technologies, CdTe has a market share of 8% in the PV industry; this exceeds all other non-silicon solar cells. Research in CdTe photovoltaics dates back to the 1950s, when the 1.5eV bandgap of CdTe material was found to be almost perfectly matched to the solar spectrum in terms of optimal conversion to electricity [1].

Due to the poor quality of n-type doping of polycrystalline (px-) CdTe, a simple heterojunction design evolved in early 60s in which p-type CdTe was matched with an n-type CdS as the window layer. Cadmium Chloride ($CdCl_2$) treatment became standard during the 70s, as it can drastically increase the solar to electrical conversion efficiency of CdS/CdTe thin film solar cells by improving the quality of px-CdTe [2]. A thin CdS layer (usually less than 200 nanometers) was developed in the 1990s to allow more photons to reach the CdTe absorber, thus resulting in 15% conversion efficiency [3]. Transparent Conducting Oxide (TCO) layers were also introduced to CdTe technology to facilitate the lateral movements of carriers across the top of the cell. The efficiency record of polycrystalline CdTe technology has been frequently updated in the recent years, and has reached 22.1% for solar cells and 18.6% for large area PV modules, surpassing the records for px-Si technologies [4].

1.2 MOTIVATION OF THIS WORK

The record efficiencies of thin-film CdTe technology are still ten absolute percent lower than the Shockley-Queisser limit. As short-circuit current density (J_{SC}) is approaching the theoretical limit, both open-circuit voltage (V_{OC}) and fill factor (FF) are

far below the theoretical limits for most devices. Although V_{OC} larger than 0.9V have been reported for single crystal (sx-) CdTe solar cells [5], low V_{OC} still limits the performance of polycrystalline CdTe devices [6].

Since V_{OC} is a strong function of the doping concentration in the absorber layer, better understanding of doping mechanism and defect formation is necessary. Like most common dopants in px-CdTe, Copper (*Cu*) forms multiple species of defects including interstitial donors (Cu_i), substitutional acceptors on *Cd* site (Cu_{Cd}) and tightly-bounded complexes such as Cu_i-Cu_{Cd} and Cd_i-Cu_{Cd}. The resulting amount of uncompensated acceptor impurities is usually three or four orders of magnitude smaller than the total atomic *Cu* concentrations, which limits the V_{OC} of *Cu*-doped CdTe solar cells significantly [7], [8]. Figure 1.2 below shows typical doping concentrations and total Cu concentrations achieved in the CdTe absorber layer fabricated at Colorado State University through varied Cu anneal temperatures[9]. Despite the fact that atomic Cu concentrations increased from $10^{17}cm^{-3}$ to $10^{18}cm^{-3}$ with increasing annealing temperature, the free carrier (holes) concentration remained constant around $10^{15}cm^{-3}$. Similar phenomena have been reported by various other sources [10] – [13]. The low V_{OC} of px-CdTe solar cells is also believed to be due to a large defect density, and short minority carrier lifetimes in the absorber layer [14]. The self-compensated active *Cu* dopants also provide active defects (recombination centers) in CdTe material as well [15], which results in poor minority carrier lifetime, that once again connects *Cu* with the low V_{OC} found in px-CdTe PV cells.

Although total Cu concentration profiles can be measured by the secondary ion mass spectrometry (SIMS) technique [16], the concentration of different species of Cu

(mainly Cu_i and Cu_{Cd}) generally cannot be identified. Lacking a description of the transition process, the theoretical concentrations of the related defects were estimated from the charge neutrality equation with formation energies of defects obtained from First Principles calculations [17]. Given this information, gaining a better understanding of kinetics behind migration and transformation of related defects in CdTe is of crucial importance to further enhance the performance of CdTe solar cells.

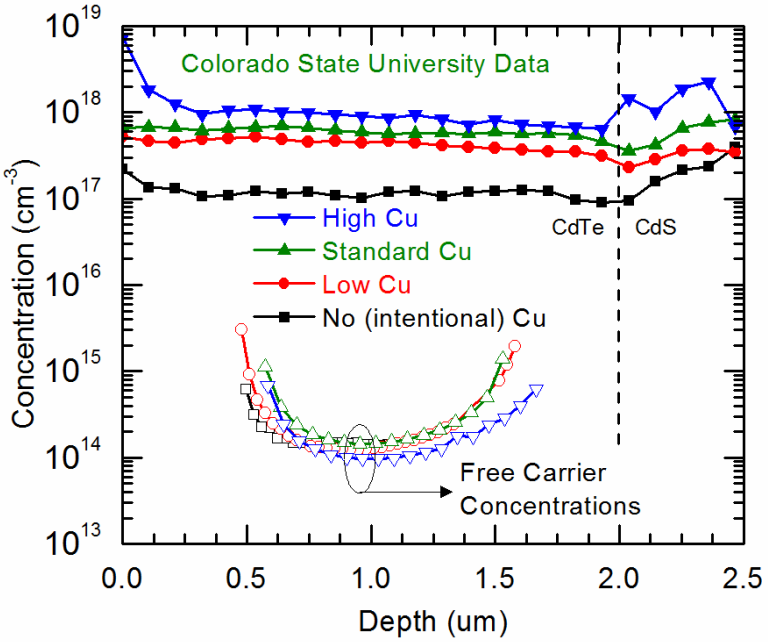

Figure 1.2. Typical Cu and free carrier concentrations presented in px-CdTe solar cells. Free carrier concentration measured by CV profiling.

Moreover, PV modules (multiple solar cells electrically connected) are expected to function properly for more than 20 years, in order to provide electricity at proper cost. However, due to the fast diffusion and reaction rates of Cu atoms, the gentle balance between mutually compensating Cu impurities could be subject to temporal or permanent changes causing metastabilities or degradation observed in CdTe solar cells [18], which

also makes the predictive simulation of device performance more important. As shown in Figure 1.3, permanent Cu depletion was found after 1000 hours of short-circuit stress at elevated temperature under 1 sun illumination, while no such behavior is observed from the open-circuit stressed sample [9]. Thus, gaining a better understanding of mechanisms that govern the formation and interactions between *Cu*-related defects is of crucial importance for further advancement of the CdTe photovoltaics.

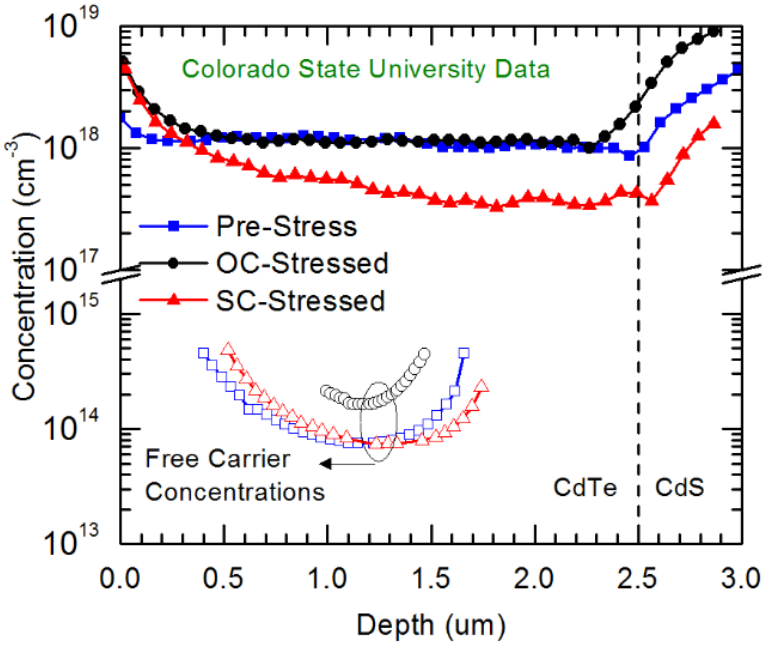

Figure 1.3. Cu migration observed from long term stress at elevated temperature. The corresponding free carrier concentration shows minor correlation to atomic Cu concentration.

Therefore a unified solver is needed, which brings multiple disciplines together as a joint effort, to address the aforementioned multi-time scale and multi-length scale issues. As depicted in Figure 1.4, the goal of such a unified solver is to eliminate the ambiguity between the observed performance changes under stress and their physical root cause by enabling a depth of modeling that takes account of diffusion and drift at the atomistic level

coupled to the electronic subsystem responsible for a PV device's function. This dissertation only focuses on Cu and Cl point defects in CdTe solar cells. Such a unified solver scheme can and should be applied to grain boundaries and other species of defects in more advanced 2D/3D simulations [19] and to other photovoltaic technologies, such as perovskite or CIGS, as well.

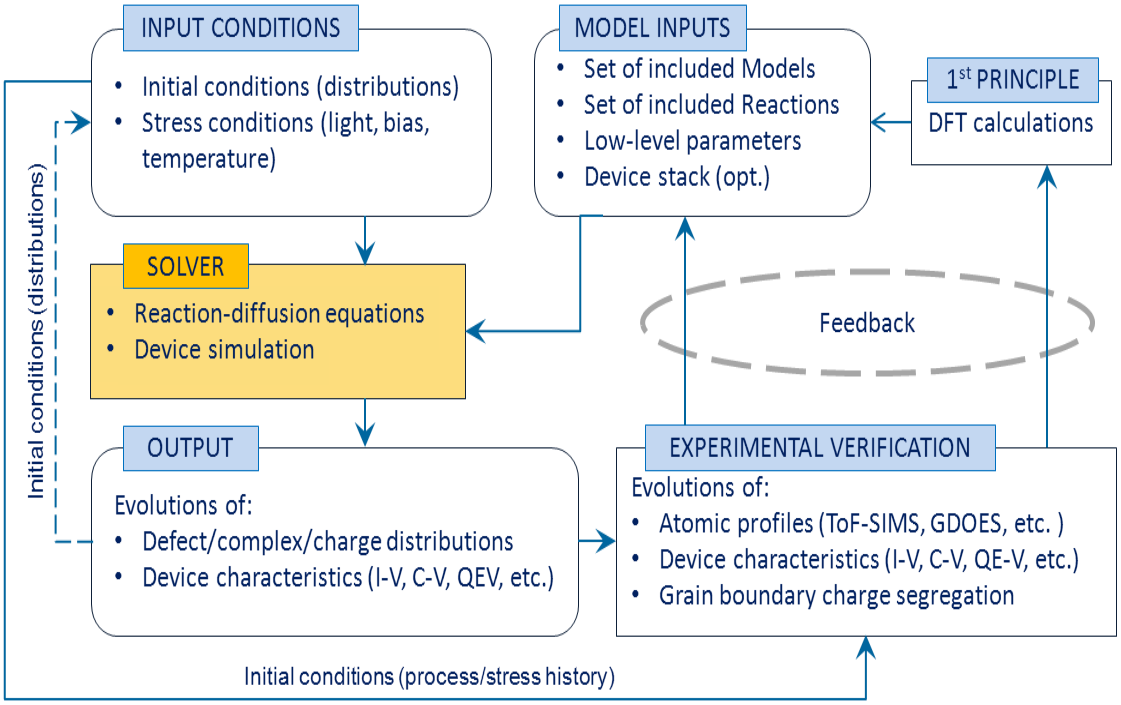

Figure 1.4. Schematic block-diagram that illustrates the use of the Unified Solver to tune the model and study CdTe device metastability.

1.3 OUTLINE OF THIS DISSERTATION

This dissertation is organized as follows.

Chapter 2 focuses on previous research related to Cu's role in CdTe solar cells. Since previous simulation effort on this topic is rather limited, we will examine recent works related to (1) theoretical calculations of the formation of Cu defects in CdTe, (2)

experimental (characterization) work on Cu related defects in CdTe, (3) metastable behavior in CdTe solar cells, and (4) previous simulation effort on Cu migration in CdTe.

Chapter 3 discusses the physical models we investigated and implemented in our simulator. In Section 3.1, the general form of the Diffusion-Reaction equations is firstly introduced. In Section 3.2, reaction models, including the calculation of reaction parameters for both the Defect-Defect reaction and the Defect-Carrier interaction is discussed in detail. In Section 3.3, the common species of Cu and Cl defects are presented. The reactions related to p-type doping formation and device metastabilities in CdTe solar cells are also discussed in this section.

In Chapter 4, the numerical methods and simulation schemes we implemented to study defect migration are described. In Section 4.1, the general coupling of device simulation and defect migration solver is presented first. With such coupling applied in the simulation, defect migration in semiconductors can be simulated accurately with real-time electric field and carrier distributions. In Section 4.2, the solution technique of the Diffusion-Reaction equations is introduced. In particular, the fully implicit reaction schemes developed specifically for this research are presented. Following this discussion, the overall simulation scheme for the Cu annealing process and device metastabilities is explained in Section 4.3.

Chapter 5 focuses on the simulation results obtained from this work. In Section 5.1, the simulated results of Cu anneal in single-crystal and poly-crystal CdTe is compared to experimental Cu profiles. Good matching was achieved between simulation and experiments, providing models and parameters in sx-CdTe material with correct physical

meanings. Qualitatively matching between simulation and experiment is achieved for poly-crystal CdTe devices, showing that our simulation, in some degree, represent the real Cu migration in CdTe solar cells. Following that, in Section 5.2, simulated device performance under long-term stress conditions is presented with experimental data. The simulated results show similar behavior to the measured device under variety of stress conditions, showing that this simulation approach is promising for predictive simulation of long-term device performance. An investigation of short-term light soaking's impact on CdTe solar cell performance is presented in Section 5.3. Qualitatively matching between measured and simulated device performance is obtained, especially when Cu-Cl interactions are included in the modeling.

CHAPTER 2

REVIEW OF LITERATURE

As Cu has been introduced into CdTe for a long time, a significant amount of experimental, theoretical and numerical research has been conducted in this area. In this chapter, we will carefully examine previous works that are related to (1) theoretical calculations of formation of Cu defects in CdTe, (2) experimental work on Cu defects in CdTe, (3) metastable behavior commonly presented in CdTe solar cells and (4) numerical simulation efforts on Cu migration in CdTe.

As CdTe is commonly used in solar cells, infrared detectors and radiation detectors for x-rays, gamma rays, beta particles and alpha particles [20], a lot of theoretical calculations were conducted for CdTe material. In 2000, Wei and his co-authors first reported using first principle calculations of defect formation energies and the defect transition energy levels of Cu_{Cd} substitutional defects in CdTe [21]. Ma et al. further derived formulas to calculate carrier density for multiple dopants in CdTe [17]. With their system, compensation (in good agreement with experimental observations) is achieved between popular Cu defects in CdTe. In 2013, Krasikov and his team showed that shallow dopants alone cannot cause the low carrier concentrations in Cl-treated CdTe samples [22]. Several other related work have been published since then [8], [23]-[25]. Yang and his colleagues also reported the multiple-barrier diffusion theory of Cui in CdTe [26]. In this work, their calculated diffusivity agrees well with experimental measurement. In 2017, Krasikov further reported the most favorable pair complexes formed in Cu-Cl doped CdTe absorber [27], as illustrated in Figure 2.1.

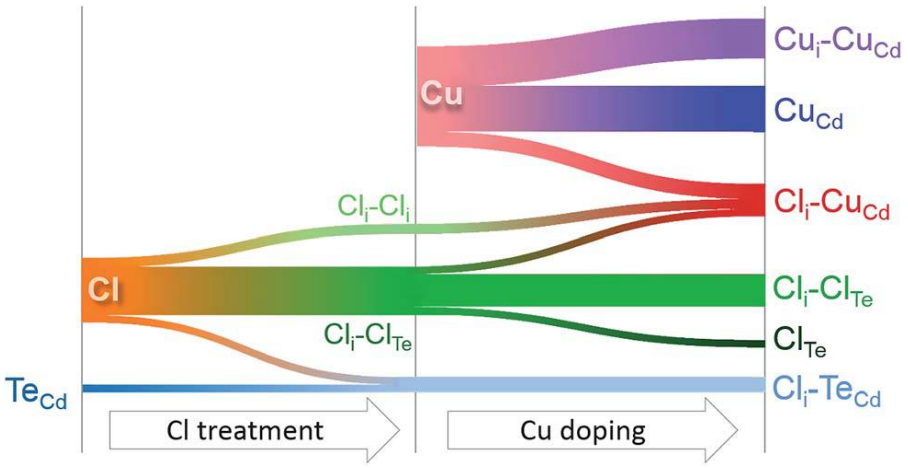

Figure 2.1. Sankey diagram qualitatively showing the defect evolution during Cl treatment and Cu doping stages. Exact concentrations and flows of defects depend on experimental conditions [27].

In the meantime, a large amount of experimental work on extrinsic defects in CdTe have been reported. Hofmann and his team first identified chlorine A centers (Cl_{Te}-V_{Cd}) in CdTe using photoluminescence [28]. The binding energy of this acceptor was estimated as 0.12 eV. Mendis et al. also used time-resolved cathodoluminescence method to capture a 47 meV shallow oxygen-related acceptor at grain boundary [29]. Recently, many experiments have been performed for Cu-related defects. Warren and his team identified two optical sub-bandgap transitions in CdTe thin-film solar cells using detailed transient photocapacitance and transient photocurrent spectroscopy measurements. One of these two defects is further identified as E_V+0.9eV Cu-related defects. Kuciauskas et al. used photoluminescence spectroscopy to study recombination in px-CdTe solar cells with V_{OC} > 0.899 V [15]. Defects with an activation energy of 0.11-0.12 eV were identified. Also this carrier lifetime limiting defect was connected to Cu_{Cd} in a second report by the same group [30].

As CdTe technology drew more and more attention in industry and academia, a lot of work has been published on its metastable behavior. Light soaking could improve the conversion efficiency of CdTe solar cells, as Ref. [31] reported. Such effect was found to be reversible upon unbiased dark storage, and ascribed to the existence of trap states in the absorber junction which depopulate when the cell is forward biased [32]. Samples also show that measured device performance can vary greatly depending on the precondition procedures, as shown in Refs. [33], [34]. The diffusion of Cu ions away from the back contact metallization in CdTe devices can explain much of the observed long-term device degradation (see Ref. [35]-[37]). The internal electric field of CdTe solar cells and Cu migration under such a field, is also demonstrated as a key factor in the degradation of CdTe devices [18]. More recently, Cu depletion is observed from CdTe cells that have been short-circuited for 831 hours at 65^{o}C [9]. While in the same experiment, no significant Cu migration is observed from open-circuit-stressed devices, which further proves that internal electric field of CdTe solar cells can also push Cu towards the back contact. Gretener and his team also reported that Cu redistribution reduces device performance by decreasing hole concentration in the absorber layer of substrate configured px-CdTe solar cells [10]. However, no significant Cu migration was presented in that work.

Traditionally, Cu migration in CdTe bulk has been treated as a pure diffusion process, described by Fick's law. In the work of Jones et al. [38], the activation energy and diffusion coefficients for Cu in CdTe were obtained by fitting experimental Cu concentration profiles obtained at different annealing temperatures with an infinite source of Cu. Teeter et al. modeled Cu migration in poly-crystalline CdTe solar cells with different solubility limits and various diffusivities with a finite source [39]. An improved version of

the two-dimensional (2D) Fisher diffusion model that accounts for segregation at the grain boundary was developed for Cu in CdTe by Akis et al [16]. In all three works, some effective Cu diffusion process was employed without atomistic mechanisms accompanying Cu diffusion. This led to a significant scatter of the obtained diffusion parameters. Thus, the reliability and predictive ability of such models is very limited. In 2016, Mao and et al. utilized Tof-SIMS to obtain high resolution 2D chemical map of polycrystalline CdTe and reported that no segregation of Cu can be detected at the grain boundaries within the sensitivities of the Tof-SIMS measurement [40].

In somewhat more detailed simulations [41], [42], drift and reactions of Group-I defects with Cd atoms were taken into account, which explained the snow plow effect causing the peak shaped profile of Group-I impurities inside single-crystal CdTe wafers. However, all such defect reactions were assumed to be in equilibrium at any moment of time. More importantly, that work focused only on the migration of Cu and Ag atoms when Cd or Te pressure is applied to single crystal CdTe wafers, but not on limited incorporation and compensation mechanism of Cu dopants that have crucial importance on the performance of CdTe solar cells.

CHAPTER 3

PHYSICAL MODELS

In this chapter, we will thoroughly examine the physical models investigated and implemented within our simulator.

3.1 DIFFUSION-REACTION EQUATIONS

The developed 1D simulator solves the diffusion-reaction equations for both free carriers and point defects.

3.1.1 Diffusion-Reaction Model

The diffusion-reaction model allows one to calculate the evolution of concentration profiles caused by reactions between different species and their fluxes [43], [44]:

$$\frac{d[X]}{dt} = -\frac{dJ_X}{dx} + R_X \tag{3.1}$$

Where R_X is the net production rate of each defect and J_X is the flux of the target defect X. Similar to the drift-diffusion model widely used in semiconductor device simulations, these fluxes are driven by the gradient of electrochemical potential which accounts for the electric potential of charged species as well as their standard formation energies. Namely, the flux expression for a species X (target defect) is of the form:

$$J_X = -D_X\left(\frac{d[X]}{dx} + \frac{[X]}{kT}\frac{d[q\varphi + G]}{dx}\right) \tag{3.2}$$

Here in Equation 3.2, D_X is the diffusivity of defect X, q stands for the electric charge carried by the species, kT is the thermal energy, φ is the electrostatic potential and G is the

spatially dependent formation energy of the defects. It is important to note that since we are dealing with Cu migration in hetero-junctions with multiple layers of different materials, the formation energy term, G, plays a crucial role on determining the segregation factor of point defects across the hetero-interface between two different materials.

3.1.2 Calculation of Reaction Rates

For typical reactions in CdTe semiconductors, including all applications in this work, two reaction prototypes based on the number of reactants, are considered: single molecular and bimolecular. For example, the forward reaction in Equation 3.3a and both directions of reaction in Equation 3.3b are bimolecular reactions and the backward reaction of Equation 3.3a is single molecular.

$$X_A + X_B \underset{K_{B1}}{\overset{K_{F1}}{\rightleftarrows}} X_C \tag{3.3a}$$

$$X_A + X_D \underset{K_{B2}}{\overset{K_{F2}}{\rightleftarrows}} X_E + X_F \tag{3.3b}$$

For convenience we will denote the production rates of species A in Equation 3.3a and 3.3b as R_A^1 and R_A^2, respectively. Although reactions involve three defects in one side of the reaction equations might be possible, the possibility of such reactions is statistically low in usual configuration of devices. The rate law is applied to calculate the reaction rates for them. For example, the production rates for species A in Equation 3.3 are written as:

$$R_A^1 = -(K_{F1} X_A X_B - K_{B1} X_C) \tag{3.4a}$$

$$R_A^2 = -(K_{F2} X_A X_D - K_{B2} X_E X_F) \tag{3.4b}$$

The rate constants for these reactions, based on the species of reactants, is discussed in the following section. And for each species of defects, the net production rate would be sum of all involved individual reactions. For example, if both Reaction 3.3a and 3.3b are involved for defect *A*, assuming sufficient reactants are provided, the instantaneous net production rate of defect *A* should be calculated as

$$R_A = R_A^1 + R_A^2 \tag{3.5}$$

3.2 REACTION MODELS

Besides differentiating the reactions based on the number of the reactants, reactions could also be divided into two types, considering whether free carriers are participating in the reactions; namely, defect-defect reactions without free carriers and defect-carrier interactions.

3.2.1 Defect-Defect Reactions

As reactions should occur between two or more reactants physically close to each other, most likely, two immobile defects located far away will not interact, even a large energy release is favored for such reactions. Moreover, due to the fact that usual concentration of extrinsic defects in CdTe thin-film devices is orders of magnitude smaller than the lattice site concentration, the mean distance between two immobile defects would be thousand times larger than the lattice constant, thus the interactions between two immobile defects are neglected in this work as well. Another limitation on the interactions is the Coulomb interactions between two charged defects. For example, if two reactants are both positively charged, the Coulomb force would prevent them from moving together,

thus the possibility of such reactions occurring is significantly lower. On the contrary, if two reactants are oppositely charged, the Coulomb force would force them to join each other within certain range. With the above limitations, defect interactions that involves two oppositely charged defects with at least one of them mobile, as in Equation 3.6, should be our primary interests.

$$X_A^{+} + X_B^{-} \leftrightarrow X_C(+X_D) \tag{3.6}$$

The reaction constant for such reactions (diffusion-limited reactions) in general is found as a function of the diffusivity, D_i, and the capture radii, R_{capt} of individual reactants [43].

$$K = 4\pi R_{capt}\left(\sum_{i=1}^{j} D_i\right)\exp\left(-\frac{E_A}{kT}\right) \tag{3.7}$$

The capture radius of this type of interactions is the balance distance between Coulomb force and the centrifugal force of the circular movement of the free mobile defect.

$$F = m\frac{v_{th}^{2}}{R_{capt}} = k_e\frac{q_1 q_2}{R_{capt}^{2}} \tag{3.8}$$

By assuming the free mobile defect is in thermal equilibrium, in which the kinetic energy of the free carrier equals to the thermal energy, we get

$$R_{capt} = k_e\frac{q_1 q_2}{m v_{th}^{2}} = k_e\frac{|q_1 q_2|}{k_B T} \tag{3.9}$$

Usually the reaction barrier energy in Equation 3.7, E_A, is set to zero in this type of reactions as no additional energy is required to move two reactants close to each other. Due to the

nature of thermodynamic equilibrium of the defect system, the reaction constant of the reverse direction of Equation 3.7 is usually described as:

$$K^b = K^f \cdot \exp\left(\Delta E^f / kT\right) \cdot n_0 \tag{3.10}$$

Note that in single-molecular reactions, n_0 is the concentration of lattice sites. For bimolecular reverse reactions, it equals one. ΔE^f, represent the energy change in the reactions, is estimated as the difference between formation enthalpies of products and reactants obtained from first-principle calculations using large supercells and the range-separated hybrid functional [27].

3.2.2 Defect-Carrier Reactions

Similarly to the single molecular reactions described in the previous session, defect-carrier reactions can also be considered as diffusion-limited reactions, as the interaction between charged defects and free carriers should be faster than the actual movement of free carriers and point defects. Moreover, the diffusion speed of free carriers should also be orders of magnitude larger than the point defects, thus the point defects can be treated as immobile in this case. Hence, the reaction constant for a charged donor capturing one free hole or for a charged acceptor capturing one free electrons and their reverse reactions (neutral dopants release free carriers), should have the same form as Equation 3.7 and 3.9:

$$K^f = 4\pi D_{eh} R_{capt} \tag{3.11a}$$

$$K^b = K^f \cdot \exp\left(-\varepsilon^{0/-1} / kT\right) \cdot N_V \cdot g_1 / g_0 \tag{3.11b}$$

Here the diffusivity of the mobile defect is replaced by the diffusivity of free carriers in the forward reaction, the ionization level of the dopant is employed as the energy barrier required to release free carriers and n_0 is replaced by the density of states with the degeneracy factor. Theoretical approach of obtaining the ionization level of the dopants is also reported in Ref. [27].

3.3 COPPER DEFECTS IN CDTE

So far, the diffusion-reaction model has only been introduced as a general numerical problem. In this session, we will discuss Cu-related defects and their interactions in CdTe material.

3.3.1 List of Defect Species

Besides the common Cu defects, as discussed in Chapter 2, including Cu interstitial, (Cu_i), Cu on Cadmium site (Cu_{Cd}), Cu complex (Cu_i-Cu_{Cd} & Cd_i-Cu_{Cd}), we are also interested in Cl-related Cu defects, such as Cl_i-Cu_{Cd} and Cl_{Te}-Cu_{Cd}, for their interactions with Cu dopants that potentially could generate doping compensation. Figure 3.1 schematically illustrated the major reactions we considered to describe Cu's migration in CdTe without presence of Cl point defects. Table 3.1 below lists the properties of major extrinsic point defects presented in this study [17], [24] – [26], [45], with the presence of both Cu and Cl species.

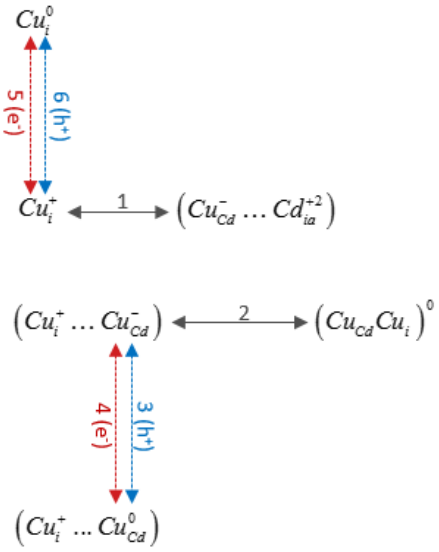

Figure 3.1. Common Cu-related reactions in CdTe material. (Courtesy of Dr. Dmitry Krasikov from First Solar)

Table 3.1. List of active defects and their properties in CdTe

Defect	D_0 (cm^2/s)	E_A (*eV*)	*Charge State*	$E_{Ionization}$ (*eV*)
$Cu_i(+)$	6.3×10^{-3}	0.46	donor	0.14
$Cu_i(0)$	3.53×10^{-3}	0.28	neutral	-
$Cu_{Cd}(-)$	-	-	acceptor	0.22
$Cu_{Cd}(0)$	-	-	neutral	-
$Cd_i(2+)$	3.21×10^{-3}	0.47	donor	0.21
Cu_i-$Cu_{Cd}(0)$	-	-	neutral	-
$Cl_{Te}(+)$	-	-	donor	0.35
$Cl_i(-)$	1.18×10^{-2}	0.89	acceptor	0.12
$Cl_i(+)$	5×10^{-4}	0.6	acceptor	0.2
$Cl_i(0)$	4.82×10^{-4}	0.28	neutral	-
Cl_i-$Cl_{Te}(0)$	-	-	neutral	-
Cl_i-$Cl_{Te}(+)$	-	-	donor	
Cl_i-$Cl_{Te}(2+)$	-	-	donor	
Cl_i-$Cu_{Cd}(0)$	-	-	neutral	-
Cl_i-$Cu_{Cd}(+)$	-	-	donor	0.17
Cl_i-$Cu_{Cd}(2+)$	-	-	donor	0.39

3.3.2 List of Reactions

In this session, we introduce the reactions that usually take place during anneal and stress conditions of Cu doped CdTe solar cells. In the figure below, we first introduce reactions between Cu defects and intrinsic CdTe defects schematically.

It is important to note that the bracket in the figure represents two isolated point defects seating close to each other, and the reactions between them do not require extra energy to bring them closer. In Table 3.2 below, the above interactions are listed with detailed calculation of their corresponding reaction constants. As Cl is commonly present in CdTe devices, Cu's interaction with Cl defects, also needs to be addressed. D. Krasikov and his colleagues at First Solar developed the theory regarding Cu & Cl-related defects reactions in CdTe. In this case an energy loop is formed among three major ClTe defects, indicating that the total entropy is conserved in our simulation. Similarly, these type of reactions, and the calculation their reaction constants are listed in Table. 3.3.

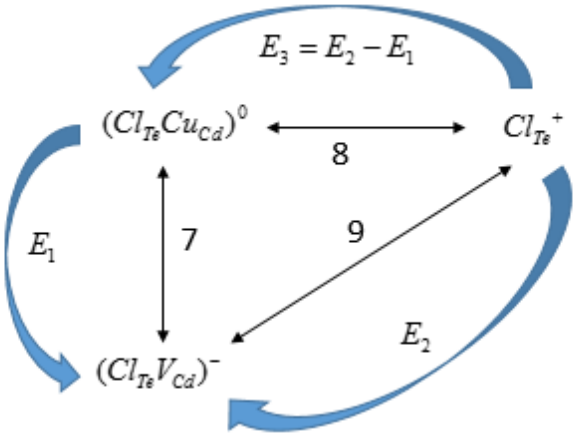

Figure 3.2. Common Cu-Cl reaction loops presented in CdTe. (Courtesy of Dr. Dmitry Krasikov from First Solar)

Table 3.2. List of Cu related reactions

NO.	*REACTION EQUATION*	*REACTION CONSTANT*
1	$Cd_{ia}^{2+} + Cu_{Cd}^{-} \underset{K^b}{\overset{K^f}{\rightleftharpoons}} Cu_i^{+}$	$K^f = 4\pi \cdot D_{0,Cd_i} \exp\left(-\frac{E_{D,Cd_i}}{kT}\right) \cdot R_{capt}^{+2,-1}$ $K^b = K^f \cdot \exp\left(\Delta E^f / kT\right) \cdot C_s$
2	$Cu_i^{+} + Cu_{Cd}^{-} \underset{K^b}{\overset{K^f}{\rightleftharpoons}} \left(Cu_{Cd}Cu_i\right)^0$	$K^f = 4\pi \cdot D_{0,Cu_i} \exp\left(-\frac{E_{D,Cu_i}}{kT}\right) \cdot R_{capt}^{+1,-1}$ $K^b = K^f \cdot \exp\left(\Delta E^f / kT\right) \cdot C_s$
3	$Cu_{Cd}^{-} + h_V^{+} \underset{K^b}{\overset{K^f}{\rightleftharpoons}} Cu_{Cd}^{0}$	$K^f = 4\pi \cdot D_h \cdot R_{capt}^{+1,-1}$ $K^b = K^f \cdot \exp\left(E_{ionization}^{Cu_{Cd}} / kT\right) \cdot g \cdot N_V$
4	$Cu_{Cd}^{0} + e_C^{-} \underset{K^b}{\overset{K^f}{\rightleftharpoons}} Cu_{Cd}^{-}$	$K^f = \sigma v_e$ $K^b = K^f \cdot \exp\left(-\frac{E_G - E_{ionization}^{Cu_{Cd}}}{kT}\right) \cdot g \cdot N_C$
5	$Cu_i^{+} + e^{-} \underset{K^b}{\overset{K^f}{\rightleftharpoons}} Cu_i^{0}$	$K^f = 4\pi \cdot D_e \cdot R_{capt}^{+1,-1}$ $K^b = K^f \cdot \exp\left(-\frac{E_{ionization}^{Cu_i}}{kT}\right) \cdot g \cdot N_C$
6	$Cu_i^{0} + h_V^{+} \underset{K^b}{\overset{K^f}{\rightleftharpoons}} Cu_i^{+}$	$K^f = \sigma v_h$ $K^b = K^f \cdot \exp\left(-\frac{E_G - E_{ionization}^{Cu_i}}{kT}\right) \cdot g \cdot N_V$

Table 3.3. List of Cu-Cl reactions.

NO.	*REACTION EQUATION*	*REACTION CONSTANT*
7	$Cl_i^- + h_V^+ \underset{K^b}{\overset{K^f}{\rightleftarrows}} Cl_i^0$	$K^f = 4\pi \cdot D_h \cdot R_{capt}^{+1,-1}$ $K^b = K^f \cdot \exp\left(E_{ionization}^{Cl_i} / kT\right) \cdot g \cdot N_V$
8	$Cl_i^0 + h_V^+ \underset{K^b}{\overset{K^f}{\rightleftarrows}} Cl_i^+$	$K^f = \sigma v_e$ $K^b = K^f \cdot \exp\left(-\frac{E_G - E_{ionization}^{Cu_{Cd}}}{kT}\right) \cdot g \cdot N_C$
9	$Cl_i^- + Cl_{Te}^+ \underset{K^b}{\overset{K^f}{\rightleftarrows}} (Cl_i Cl_{Te})^0$	$K^f = 4\pi \cdot D_{0,Cl_i} \exp\left(-\frac{E_{D,Cl_i}}{kT}\right) \cdot R_{capt}^{+1,-1}$ $K^b = K^f \cdot \exp\left(\Delta E^f / kT\right) \cdot C_s$
10	$Cl_i^+ + Cu_{Cd}^- \underset{K^b}{\overset{K^f}{\rightleftarrows}} \left(Cl_i\, Cu_{Cd}\right)^0$	$K^f = 4\pi \cdot D_{0,Cl_i} \exp\left(-\frac{E_{D,Cl_i}}{kT}\right) \cdot R_{capt}^{+1,-1}$ $K^b = K^f \cdot \exp\left(\Delta E^f / kT\right) \cdot C_s$
11	$\left(Cl_i\, Cu_{Cd}\right)^0 + h_V^+ \underset{K^b}{\overset{K^f}{\rightleftarrows}} \left(Cl_i\, Cu_{Cd}\right)^+$	$K^f = \sigma v_h$ $K^b = K^f \cdot \exp\left(-\frac{E_G - E_{ionization}^{Cl_i Cu_{Cd}}}{kT}\right) \cdot g \cdot N_V$
12	$\left(Cl_i\, Cu_{Cd}\right)^+ + h_V^+ \underset{K^b}{\overset{K^f}{\rightleftarrows}} \left(Cl_i\, Cu_{Cd}\right)^{2+}$	$K^f = \sigma v_h$ $K^b = K^f \cdot \exp\left(-\frac{E_G - E_{ionization}^{Cl_i Cu_{Cd}}}{kT}\right) \cdot g \cdot N_V$

13	$Cl_i^+ + e^- \underset{K^b}{\overset{K^f}{\rightleftarrows}} Cl_i^0$	$K^f = 4\pi \cdot D_e \cdot R_{capt}^{+1,-1}$ $K^b = K^f \cdot \exp\left(-\frac{E_{ionization}^{Cl_i}}{kT}\right) \cdot g \cdot N_C$
14	$Cl_i^0 + e_C^- \underset{K^b}{\overset{K^f}{\rightleftarrows}} Cl_i^-$	$K^f = \sigma v_e$ $K^b = K^f \cdot \exp\left(-\frac{E_G - E_{ionization}^{Cl_i}}{kT}\right) \cdot g \cdot N_C$

The actual reactions involved in our simulations include, but are not limited to these ten reactions. For example, as one of the most common intrinsic defects in CdTe, Cd vacancies, are not discussed in this work, despite the fact that they are usually included in simulations. However, the effect of V_{Cd} may not be that significant as its concentration is usually not that high and the major reaction it participates in, such as the formation of Cu_{Cd} from Cu_i and V_{Cd}, does not convert donors or neutral defects into acceptors. Hence, it is not discussed in this dissertation.

CHAPTER 4

NUMERICAL MODELS AND SIMULATION SCHEME

In this chapter, we will focus on the numerical solutions of the self-consistent diffusion-reaction simulator.

4.1 SOLVING DIFFUSION-REACTION EQUATIONS

In the previous chapter, we already introduced the generalized form of diffusion-reaction equations, as Equation 3.1 and 3.2 described. However, in order to reduce numerical artifact, and to achieve convergence between fast reactions and "slow" diffusions, a split scheme is applied to solve the diffusion-reaction scheme. In detail, a fully implicit reaction simulator was isolated from drift-diffusion equation to avoid negative concentration of point defects and to achieve conservation of total atoms. However, for the device simulation part, no such splitting is employed as only current is required to be conserved in semiconductor devices, but not free carriers, due to boundary conditions and recombination-generation term of free carriers in drift-diffusion model simulator. Thus, two isolated equations serve as the general diffusion-reaction equation [19]:

$$\frac{d[X]}{dt} = -\frac{dJ_X}{dx} \tag{4.1}$$

$$\frac{d[X]}{dt} = R_X \tag{4.2}$$

Usually the drift-diffusion equations are solved after the reaction part, in order to allow drift-diffusion process of mobile defects before device simulation.

4.1.1 Solution of Drift-Diffusion Equations

To solve the drift-diffusion equation, one need to discretize the continuity equations first. Schafetter-Gummel discretization scheme [46] is employed to solve the drift-diffusion equations with acceptable linear potential variation between neighboring mesh points. Thus, by using half-point difference scheme, Equation 4.1 can be rewritten as:

$$\frac{d[X]}{dt} = -\frac{dJ^X}{dx} = \frac{J^X_{i-1/2} - J^X_{i+1/2}}{(dx_{i-1} + dx_i)/2} \tag{4.3}$$

Where the superscript X denotes the species of defects X, subscript i (and i-1, i+1/2 and i-1/2) represent the number of the grid point. For example, $J^X_{i+1/2}$, indicating the flux of the defect X goring from grid point i to grid point i+1, should be calculated by the standard drift-diffusion equations (as shown in Equation 3.2)

$$J^X_{i+1/2} = -D^X_{i+1/2}\left(\frac{X}{kT}\frac{d[\phi]}{dx} + \frac{d[\mathrm{X}]}{dx}\right) \tag{4.4}$$

Where ϕ denotes the sum of electrical potential and standard Gibbs energy of formation of defect X:

$$\phi = q\varphi + G \tag{4.5}$$

In Equation 4.5, q denotes the charge of the defects. By inserting $X = X'\exp(-\frac{x - x_i}{A})$ into Equation 4.4, we could get $A = -D^X/\phi_i$, $X = X'\exp(-\phi_i \frac{x - x_i}{D^X})$ and

$$J_{i+1/2}^{X} = -D_{i+1/2}^{X} \frac{dX'}{dx} \exp(\phi_i (x_{i+1} - x_i) / D^X) \tag{4.6}$$

Hence, moving the exponential term into the LHS and integrating this equation from x_i to x_{i+1}, we get

$$J_{i+1/2}^{X}(1 - \exp(-\phi_i dx_i / D^X)) = -\phi_i \frac{X_{i+1} - X_i \exp(\phi_i dx_i / D^X)}{\exp(\phi_i dx_i / D^X)} \tag{4.6}$$

Therefore, the drift-diffusion model defect flux can be written as,

$$J_{i+1/2}^{X} = -\frac{D_{i+1/2}^{X}}{dx_i}(X_{i+1} B\left(\frac{\phi_{i+1} - \phi_i}{V_T}\right) - X_i B\left(\frac{\phi_i - \phi_{i+1}}{V_T}\right)) \tag{4.7}$$

$$J_{i-1/2}^{X} = -\frac{D_{i-1/2}^{X}}{dx_{i-1}}(X_i B\left(\frac{\phi_i - \phi_{i-1}}{V_T}\right) - X_{i-1} B\left(\frac{\phi_{i-1} - \phi_i}{V_T}\right)) \tag{4.8}$$

Where B is the Bernoulli function. Substituting Equation 4.7 and 4.8 into Equation 4.3, gives the following equation that allows one to calculate the changes of defect concentration caused by drift and diffusion

$$\frac{d[X]}{dt} = \frac{\frac{D_{i+1/2}^{X}}{dx_i}(X_{i+1} B\left(\frac{\phi_{i+1} - \phi_i}{V_T}\right) - X_i B\left(\frac{\phi_i - \phi_{i+1}}{V_T}\right)) - \frac{D_{i-1/2}^{X}}{dx_{i-1}}(X_i B\left(\frac{\phi_i - \phi_{i-1}}{V_T}\right) - X_{i-1} B\left(\frac{\phi_{i-1} - \phi_i}{V_T}\right))}{(dx_{i-1} + dx_i)/2} \tag{4.9}$$

Applying time discretization,

$$\frac{d[X]}{dt} = \frac{X_i^{new} - X_i^{old}}{\Delta t} \tag{4.10}$$

where Δt is the time step interval. One can get the discretized continuity equation as follows

$$
\begin{aligned}
&A_i \cdot [X_{i-1}^{new}] + B_i \cdot [X_i^{new}] + C_i \cdot [X_{i+1}^{new}] = F_i \\
&F_i = \frac{2 \cdot D_{i-1/2}^X}{dx_{i-1}(dx_i + dx_{i-1})} B(\frac{\phi_{i-1} - \phi_i}{V_T}) \\
&B_i = -\frac{2}{dx_i + dx_{i-1}} (\frac{D_{i-1/2}^X}{dx_{i-1}} B(\frac{\phi_i - \phi_{i-1}}{V_T}) + \frac{D_{i+1/2}^X}{dx_i} B(\frac{\phi_i - \phi_{i+1}}{V_T})) - \frac{1}{\Delta t} \\
&C_i = \frac{2 \cdot D_{i+1/2}^X}{dx_i(dx_i + dx_{i-1})} B(\frac{\phi_{i+1} - \phi_i}{V_T}) \\
&F_i = -\frac{[X_i^{old}]}{\Delta t}
\end{aligned}
\tag{4.11}
$$

Many solution techniques can be employed to solve this set of partial differential equations. As in our case, both LU decomposition and MATLAB Backslash (direct inverse of the coefficient matrix) work fine with this scheme. These two solution techniques are identical.

4.1.2 Solving Reactions Implicitly

Here we describe the solution techniques for implicit reactions. There are two major reasons for a split implicit reaction simulator in this work: (1) to achieve conservation of total atoms, (2) to avoid negative concentration of point defects.

If point defects are treated with explicit schemes, such as SRH recombination of free carriers in drift-diffusion equations, large reaction terms may cause negative concentration of point defects when time step is large. For example, let us consider one artificial case, where reactant X_1 is transferring into resultant X_2 with reaction constant K_f. For simplicity of this example, the reverse reaction constant, K_b, is neglected or can be considered as infinitely small.

$$X_1 \underset{K_b}{\overset{K_f}{\rightleftarrows}} X_2 \tag{4.12}$$

Using explicit scheme, one can arrive at

$$X_1^{j+1} = X_1^{j} - K_f \cdot \Delta t \cdot X_1^{j} = X_1^{j} \cdot (1 - K_f \cdot \Delta t) \tag{4.13}$$

Where the superscripts j and j+1 represent time step j and the next time step j+1. This equation is only valid when $K_f \cdot \Delta t$ is smaller than 1, otherwise negative concentration of X_1 will be presented at time step j+1. Although time step can be calculated based on the reaction constants, for our case, where multiple reactions are running with reaction rates varied with orders of magnitude, limiting slow reactions with the smallest time step are not a practical option. Thus, an implicit reaction scheme that is guaranteed to perform reactions without leading to negative concentrations is required.

If we could calculate the net reactions based on X_1 of time step j+1 but not X_1 of time step j, usually called implicit scheme, X_1 will always be positive regardless of the reaction constant and time step:

$$X_1^{j+1} = X_1^{j} - K_f \cdot \Delta t \cdot X_1^{j+1} \tag{4.14}$$

$$X_1^{j+1} = \frac{X_1^{j}}{1 + K_f \cdot \Delta t} \tag{4.15}$$

It is important to note that such implicit scheme is employed only to avoid negative concentrations for reactions with large value of the $K \cdot \Delta t$ product, but not to calculate such reactions accurately. To calculate fast reactions precisely, smaller Δt is required. Such

scheme would benefit us when multiple reactions with huge difference in reaction rates are presented in simulations. With the implementation of implicit scheme, the time step would only be limited by the most important reaction, which usually is the reaction with largest reaction rate but not largest reaction constant. The other reactions, usually with low concentration of reactants, could be calculated with the numerically stable implicit scheme regardless of the choice of the time step.

The same implicit scheme can be applied to reactions with multiple reactants. Let us consider the single molecular reaction given by Equation 3.1

$$\begin{aligned} &X_i \underset{K_B}{\overset{K_F}{\rightleftharpoons}} X_j + X_k, \\ &\Delta X_i = K_B X_j X_k - K_F X_i \\ &\Delta X_j = K_F X_i - K_B X_j X_k \\ &\Delta X_k = K_F X_i - K_B X_j X_k \end{aligned} \tag{4.16}$$

This could, for instance represent the knock-off reaction described by Reaction 1 in Table 2, where interstitial Cu replaces lattice cadmium, resulting in Cu_{Cd} and an interstitial cadmium atom. Note that the number of total atoms are conserved here. Using Implicit Euler method, we could write the first ODE for time step Δt as an algebraic expression

$$\frac{1}{\Delta t}(X_i^{t+1} - X_i^{t}) = K_B X_j^{t+1} X_k^{t+1} - K_F X_i^{t+1} \tag{4.17}$$

Since Δt should be small, we move it to the RHS to avoid numerically unstable division by a small number.

$$X_i^{t+1} - X_i^{t} = (K_B X_j^{t+1} X_k^{t+1} - K_F X_i^{t+1})\Delta t \tag{4.18}$$

Using our conservation laws, we can also write X_j and X_k in terms of X_i from time step t+1 and t

$$\begin{aligned} X_j^{t+1} &= X_j^t + X_i^t - X_i^{t+1} \\ X_k^{t+1} &= X_k^t + X_i^t - X_i^{t+1} \end{aligned} \tag{4.19}$$

Substitution yields

$$X_i^{t+1} - X_i^t = K_B \Delta t (X_j^t + X_i^t - X_i^{t+1})(X_k^t + X_i^t - X_i^{t+1}) - K_F \Delta t X_i^{t+1} \tag{4.20}$$

Further derivation reveals that this is a quadratic equation for X_i^{t+1}. Rearrangement and expansion yields the three coefficient as

$$\begin{aligned} &A \cdot (X_i^{t+1})^2 + B \cdot X_i^{t+1} + C = 0 \\ &A = K_B \Delta t \\ &B = -(1 + K_F \Delta t + K_B \Delta t (2X_i^t + X_j^t + X_k^t)) \\ &\mathrm{C} = X_i^t + K_B \Delta t (X_i^t + X_j^t)(X_j^t + X_k^t) \end{aligned} \tag{4.21}$$

We can then use the quadratic formula to yield

$$X_i^{t+1} = \frac{-B \pm \sqrt{B^2 - 4AC}}{2A} = \frac{2C}{\sqrt{B^2 - 4AC} - B} \tag{4.22}$$

Again, A is removed from the denominator to avoid unstable division by a small number as it is proportional to Δt. Since B is always negative for positive concentrations, we can also determine the appropriate sign of the square root to obtain our final solution.X_j^{t+1} and X_k^{t+1} can be calculated by Equation 4.11 with updated X_i.

Similarly, bimolecular reactions can be discretized using Implicit Euler method and conservation laws in the same manner as the single molecular reactions.

$$X_i + X_j \underset{K_B}{\overset{K_F}{\rightleftharpoons}} X_k + X_l \tag{4.23}$$

A quadratic equation can be obtained, with the following coefficients.

$$\begin{aligned} &A\cdot(X_i^{t+1})^2 + B\cdot X_i^{t+1} + C = 0 \\ &A = (K_B - K_F)\Delta t \\ &B = -1 - K_F\Delta t(X_j^{t} - X_i^{t}) - K_B\Delta t(2X_i^{t} + X_k^{t} + X_l^{t}) \\ &\mathrm{C} = X_i^{t} + K_B\Delta t(X_i^{t} + X_k^{t})(X_i^{t} + X_l^{t}) \end{aligned} \tag{4.24}$$

Solution of this equation is given by Equation 4.14.

4.1.3 Iteration by Reactions and Common Source of Error

Since reactions are isolated from the drift-diffusion equations, we no longer need to calculate the net production rate of each point defect as Equation 3.4 does. Instead, the implicit reaction scheme solves reactions by pairs. Hence, reactions are performed iteratively pair by pair in this work. Figure 4.1 shows the detailed flow chart of the diffusion-reaction solver with iteration of reactions. In general, in each time step, reactions are performed by pairs prior to the calculation of drift-diffusion of each species of defects, or wise versa. Many numerical experiments were conducted in order to understand the accuracy of this particular approach, such as switching orders of drift-diffusion reaction, switching orders in reaction iteration and simulations with different time step. The conclusion is that errors could be introduced with two different mechanisms, especially when larger timestep is involved.

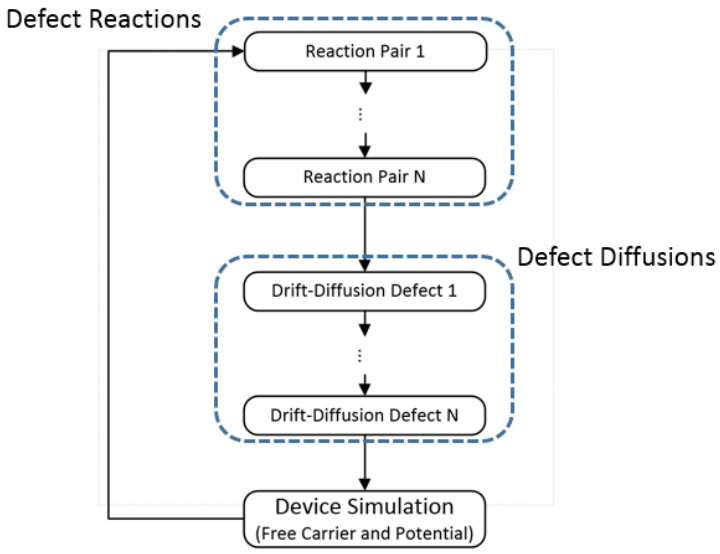

Figure 4.1. Flow chart of the Diffusion-Reaction part of this solver.

First source of these error is the iteration of reaction itself when non-appropriate timesteps were employed. Figure 4.2 below shows three 0-D reaction simulation using different time steps. With time evolution, larger time steps started to generate discrepancies comparing to the case with smallest timestep. The simulation fails due to a particular single participant chain reaction presented in this test case:

$$A \leftrightarrow B \leftrightarrow C \tag{4.1}$$

Due to fast A to B and very fast B to C process, B can be treated as catalyst in one reaction with slow forward reaction rate.

$$A \xrightarrow{B} C \tag{4.2}$$

Due to the reaction in pair procedure, this linear reaction was separated into two reactions in this approach, and the overall reaction rate from A to C hence is limited by the intermiediate product B. In extreme cases, where even more intermiediate products are

present, like Figure 4.2 depicts, poor timestep selection could cause slower A to B transition (and potetentially B to C, C to D transition in a chain). Thus, due to implicit scheme's nature, questionable concentration of the final product is obtained. Despite this potential error introduced in this extreme cases, no significant error was observed in simulation with realistic Cu and Cl defects, where typical reaction time constant is around mili-second level and no long chain reaction is present.

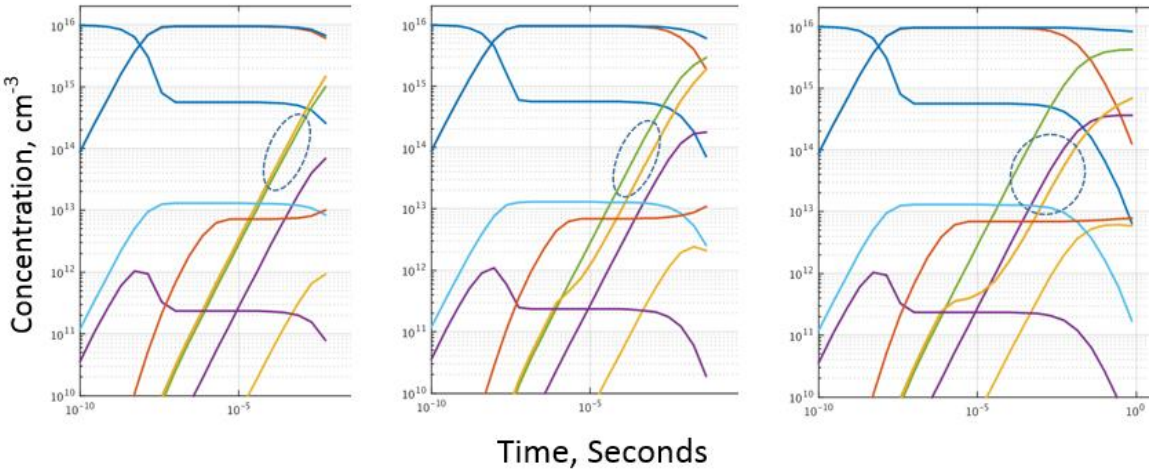

Figure 4.2. A test case with long chain reactions where iteration scheme fails. Timestep increased from 0.1ns to 1ns and 10ns from left to right.

Another common source of error is the coupling between reaction and drift-difusion solvers, especially when fast mobile ions are also presented in fast reaction. In reality, both reaction and migration of point defects should be progressing continuosly but in simulations, due to time domain discretization, such statement may not hold. Assume the same reaction discussed earlier in this section, where defect A converts to C with B as intermediate state. For extreme cases where B is a fast diffuser, determine the ratio of defect B being drifted or transitioned into C is of crucial importance in the accuracy of simulations.

As defect reactions are usually orders of magnitude faster than drift-diffusions of defects in this research, limiting the simulation timestep by reaction works well in this research work.

4.2 COUPLING BETWEEN DEVICE SIMULATION AND DEFECT MIGRATION

4.2.1 General Two-Loop Scheme

The most important feature of this numerical simulator is the coupling achieved between device simulation and diffusion-reaction of defects. Coupling these two parts enables one to simulate defects migration with real-time electrostatic environment, especially for charged interstitials such as $Cu_i(+)$ and $Cl_i(-)$ in this particular research. A two-loop scheme is applied to couple device simulations and defect migrations in this work [47]. One outer loop is employed to handle diffusion and reactions of the defects, with time step determined by the rate of reactions and diffusions, while another inner loop is applied to solve the steady states of the device (or bulk) based on the defect distribution calculated from the outer loop. Figure 4.3 schematically illustrates the flow chart of the simulator.

In the inner loop, we are solving drift-diffusion model, in which Poisson's equation and the continuity equations for electrons and holes are solved self-consistently using Gummel's iteration method [48]. It should be noted that the drift-diffusion equations describing the evolution of free carriers, have the same mathematical form as those describing the migration of point defects.

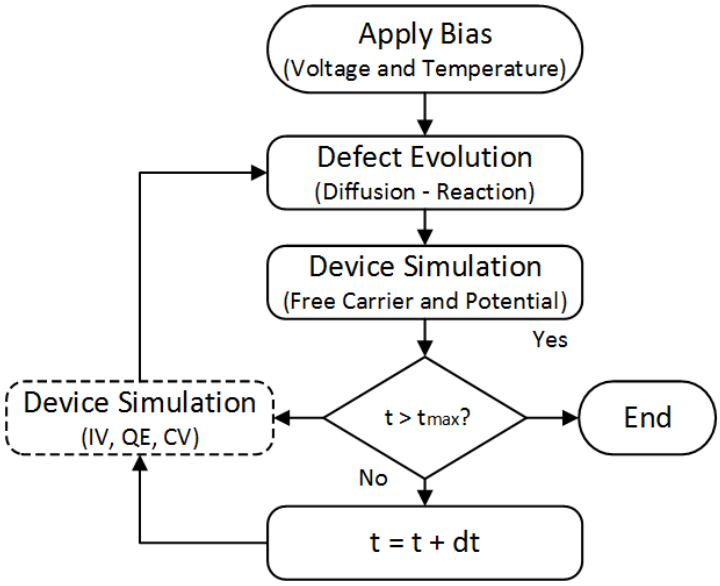

Figure 4.3. Schematic Flowchart of the simulator.

4.2.2 Defect Migration Induced Oscillation in Simulation

As point defects, especially charged mobile interstitials, respond to real-time electrostatic potential obtained from steady-state device simulation, small spatial variation in electro-potential potential could grow into strong oscillations, both in time domain and in spatial domain. Such phenomena is more commonly observed and has been well studied for free carriers (which can also be treated as charged mobile point defects) in numerical simulation of submicron semiconductor devices [49]. To handle such problems, mesh size should be limited by Debye length and time step by the dielectric relaxation time. Similarly to electrons and holes, the dielectric relaxation time constants for point defect is calculated as following:

$$\tau_D = \frac{\varepsilon}{qND/(k_B T)} \tag{4.1}$$

where ε is the dielectric constant, q is the charge of the defect, N is the concentration, D is the diffusivity, k_BT is the thermal energy. Based on the preliminary parameters employed in this research, Figure 4.4 shows the dielectric time constant that is able to deliver little or none oscillation in CdTe with different amount of ions at different temperature conditions. Assuming 10^{16} cm^{-3} is the common concentration of mobilized $Cu_i(+)$ and $Cd_i(+)$, time step small as 10us or 1ms should be applied to avoid oscillations in 300°C annealing or 100°C stress simulations.

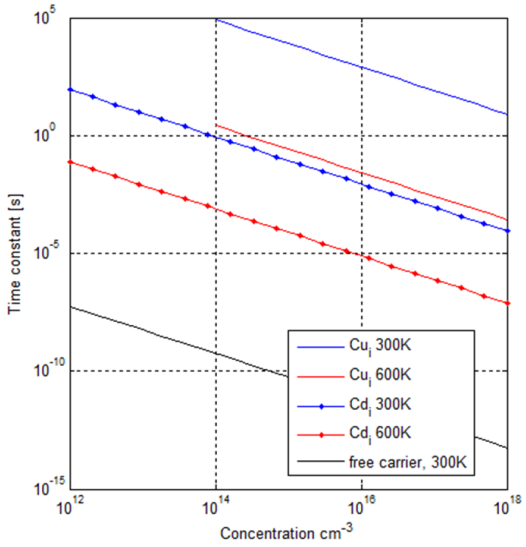

Figure 4.4. Time steps required for oscillation-free simulations with different amount of ions at different temperatures. Black line is for electrons with $100cm^2/Vs$ mobility.

Such numbers are not practical for meaningful simulations of neither tasks, as millions of time steps would be required for a 10 minutes annealing or 30 hour stress. Furthermore, such time step requirement is employed to limit mobile ions transport between neighboring mesh points [49]. Increase in spatial mesh size, by breaking Debye length limits, which could significantly reduce such transport, helps to further relax time

step requirement in theory. But, mesh size also plays important role in convergence and accuracy of the device simulation part [48], thus limited effort was performed to increase time step in this direction. Instead, two other approaches were investigated and applied in this work.

Since these oscillations are usually triggered by small spatial variation in electrostatic potential, apply smooth electric field for the drift of mobile ions helps to reduce oscillation. Particularly, Ohmic contact / Dirichlet boundary condition that are directly applied to CdTe absorber layer, creating variations near the boundary, should be avoided. Figure 4.5 shows a typical boundary oscillation caused by defect migration and Dirichlet boundary conditions in simulations. In this case, concentration of 10^{17} cm^{-3} immobile acceptors was uniformly distributed in the absorber layer. For mobile donors (usually $Cu_i(+)$ in CdTe), Dirichlet boundary condition is applied to assume an infinite source of the same 10^{17} cm^{-3} concentration. Ohmic contact / Dirichelt boundary condition was applied in device simulation, where electrostatic potential at the boundary was pinned at intrinsic level due to charge neutralization in this case. In the figure, mobile donor concentration at the second mesh point is plotted against time evolution with different time steps applied. As illustrated, oscillations occurred when donor concentration is getting close to acceptor, where net donor concentration is minimum and tiny changes in its value could cause large potential variations. As shown on the top panel, increasing time step to 5 times dielectric relaxation time constant results in unresolved oscillation while the simulator handles smaller time steps more adequately. On the bottom plot of Figure 4.5, where larger spatial mesh size was applied, same simulation can utilize larger time steps.

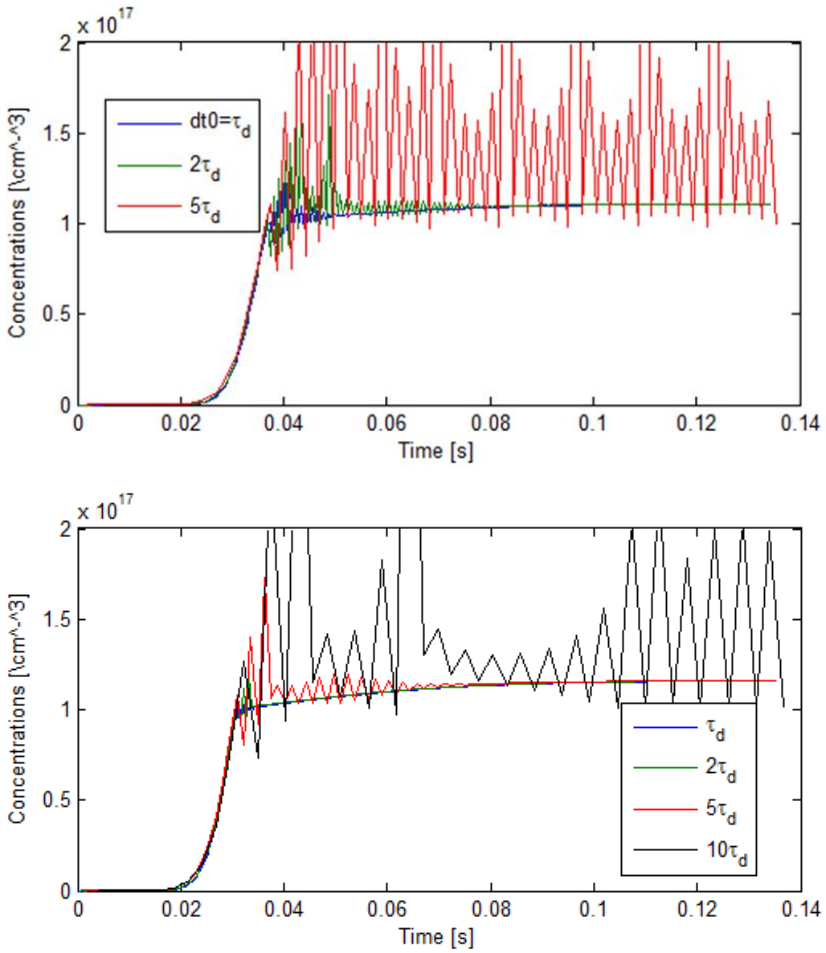

Figure 4.5. Typical defect migration induced oscillations in simulation. Top: small mesh size (5nm) requires dielectric relaxation time to overcome oscillation. Bottom: larger (5x) time step can be applied with larger spatial mesh size (20nm).

To solve this issue, buffer layer at the boundary is introduced in this research to avoid pinning potential and mobile donor concentration at the CdTe boundary. With a buffer layer, both electrostatic potential and mobile ions concentration at the CdTe surface are flexible, thus the chances of them creating spatial variations could be significantly reduced. No quantitative investigation was conducted on the effect of applying these buffer layers. In the next section, using this buffer layer as Cu source and back contact of CdTe

solar cells will also be addressed. From another perspective, due to the flip-flop nature of these migration-induced-potential-change-induced-migration problem, simply reduction of the potential update between neighboring time steps by 50% could significantly decrease mobile ions response to oscillating potentials, especially when perfect flip-flops are invoked. Such approach is semi-empirical but effective.

However, as non-uniform mesh and more than one species of mobile charged ions are usually employed in real simulations, calculation of the proper time step of multiple species at different mesh points is practical but impacts the overall efficiency of simulations, because the simulator usually can handle time steps a couple of times larger than that time constant. Using 50% potential update further relaxes the time step limitation. Simply applying the smallest dielectric relaxation time constants expense too much unnecessary computational power. Thus, a more practical approach was employed: simulation usually starts with a smaller time step, in millisecond scale, to avoid devastating oscillations at the beginning of simulations. Based on the status of the simulation, time steps are automatically increased by a factor (for example, 2 times) after a few thousands of time steps. Once oscillations are detected, time step is decreased by the same factor to accommodate small dielectric relaxation time constants appeared in the system. In detail, usually it takes 10 to 20 time steps to stabilize oscillations if appropriate time step was applied. If not, extra reduction of time step will be performed until stabilization is achieved. Although this particular empirical scheme works well in this research, more advanced implicit schemes should be able to further reduce oscillations and related computational burdens.

4.2.3 Automatic Damping in Device Simulations

Similarly to the oscillation problems induced by this self-consistent coupling of mobile dopants and electrostatic potentials, free carriers, electrons and holes more specifically, can also create divergence in device simulations. Due to high mobility of dopants, in this particular research, where non-inform, or even worse, abrupt doping profiles are commonly presented, such issue is further raised.

In a standard device simulation, as dopant profile is typically fixed, damping scheme, for example 50% update between Gummul iterations, can be employed to solve this issue [50]. On the contrary, in these coupled dynamic simulations, dopant profile evolves with time, thus there is no single damping factor to solve all the problems with acceptable efficiency. Given this, automatic damping scheme is implemented in the device simulator to handle such critical issue: damping factors will only be introduced to the device simulator once divergence is detected. Stronger damping between Gummel iterations will be applied if the simulator still failed to converge. The limitation on number of Gummel iteration allowed in each device simulation is increased accordingly. After several reinforcements of damping factors and number of Gummel iterations, solver will move onto next time step with the best "converged" solution regardless of whether it truly meets convergence requirement, which is usually 10^{-7} eV maximum potential updates in the entire simulation domain. In most cases, a couple of diverged time steps does not significantly impact an extended simulation with more than thousands of time steps. However, if there is no such limitation, consecutive diverged time steps eventually could destroy simulations by creating mobile defect oscillations or simply drive the system into

non-physical electrostatic potentials and deadly loops. Figure 4.6 and 4.7 below show two different simulation cases with both oscillation detection and automatic damping for device simulation part. These plots illustrate the time interval and number of iterations required for each time steps in an annealing simulation at 350^{o}C and a stress simulation for device stressed at 65^{o}C.

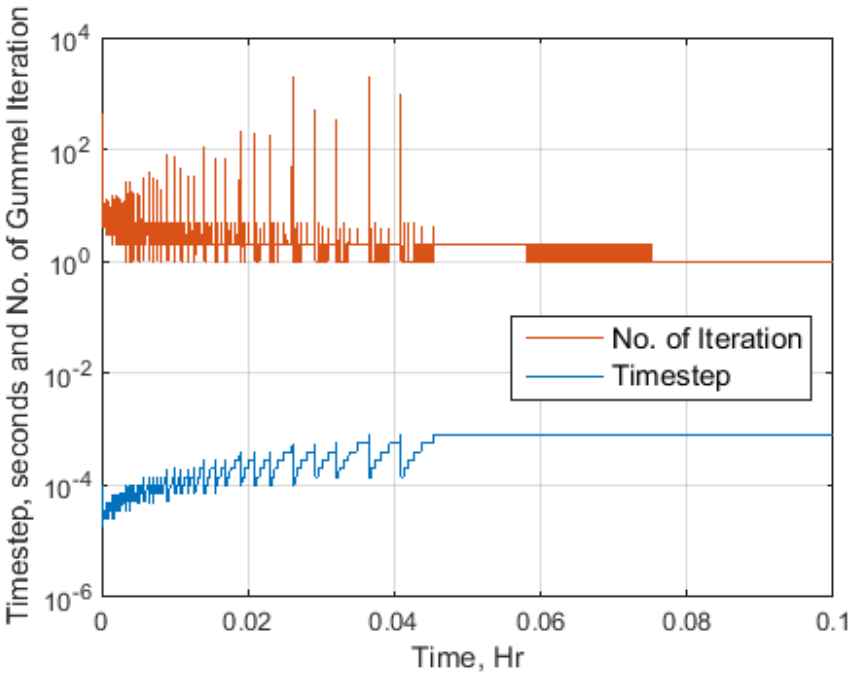

Figure 4.6. Typical defect migration induced oscillations and automatic damping involved in a 350^{o}C annealing simulation.

In Figure 4.6, each spikes of No. of Iteration represents diverged device simulations strengthen damping with extra Gummel iterations to obtain convergence. On the other hand, a general trend of increasing timestep is presented, with multiple occasions of oscillation invoked timestep reduction. It is interesting to find that sudden divergent device simulation is highly synchronized with oscillation detection. Most likely the divergence is caused by

oscillated defect migration thus once defects are stabilized, device simulation starts working smoothly with minor variations in iteration numbers. In the 65°C stress simulation demonstrated in Figure 4.7, gradual increment of time step is presented without any oscillation being detected. However, spikes of iteration number are observed during light/bias conditions switching. Also, a large portion of the time steps following condition changes required extra iteration to achieve convergence in device simulation, which is probably caused by doping profile changes in response to different light/bias conditions. Both samples show the importance of dynamic time step in defect migration and automatic damping in device simulation. To deliver smooth/uninterrupted simulation results, both techniques are necessary.

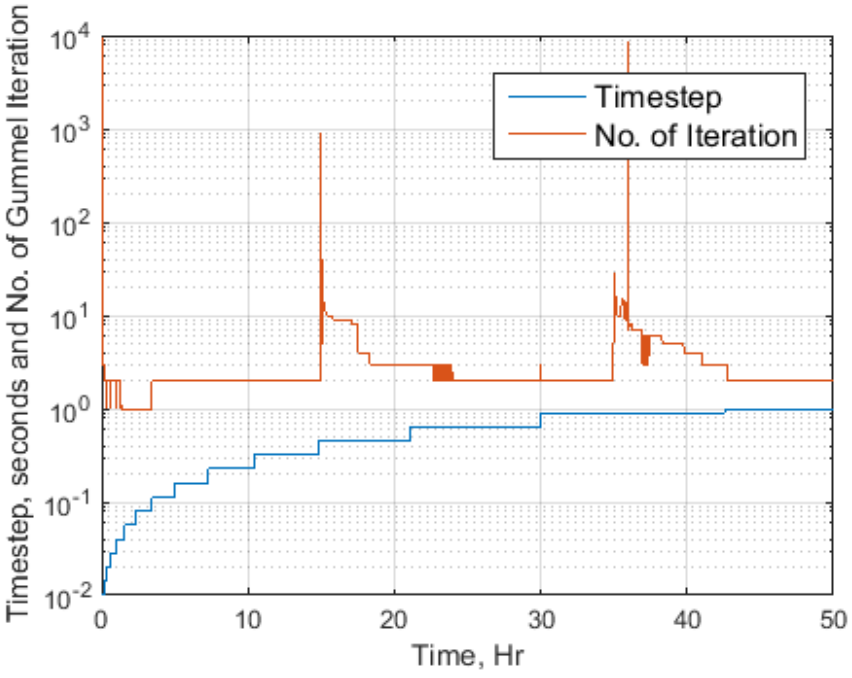

Figure 4.7. Automatic damping involved in a 65°C stress simulation with changing light/bias conditions.

4.3 SIMULATION SCHEMES

In this section, we will discuss the general schemes adopted in the solver for different types of simulation task.

4.3.1 Discussions on Cu source layer

Regardless of whether Cu is introduced in sx-CdTe wafer or px-CdTe prepared for solar cell applications, the incorporation of Cu in CdTe is usually achieved by thermal treatment or anneal following the deposition of Cu source layer. For the deposition of Cu layer, common procedure includes ZnTe:Cu co-evaporation [51], [52], CuCl treatment [9] and Cu/Au paste [53], [54]. In some cases, the Cu source layer would also serve as buffer layer or contact layer after the thermal treatment [52], [55], [56]. While for some others, for example CuCl treatment, the source layer is removed prior to the application of back contact in order to eliminate excess Cu in CdTe for long term stability of the device [9], [57]. In general, controlled activation of Cu is essential to achieve quality CdTe solar cells.

Thus, a Cu source layer is usually assumed in our simulations. To simplify the complexity of this work, only ZnTe:Cu layer is considered as the source layer in both anneal simulations and long term migration simulations, due to better knowledge of the properties of ZnTe:Cu. The variance between Cu source layers, most importantly the initial Cu_i injection concentration in CdTe, could be achieved in the assumed ZnTe:Cu layer by adjusting Cu source concentration, formation energies of Cu and even doping concentration in ZnTe. Hence, the employed ZnTe:Cu layer could effectively serve as other Cu source in terms of Cu migration. As for the electronic properties of these buffer\contact layers, such assumptions may not hold. However, as the primary goal of this research is

about Cu migration in CdTe, the electronic properties of the buffer/contact layer may not be that important. Figure 4.8 below schematically illustrated the migration progress of Cu atom from the source layer into the CdTe bulk.

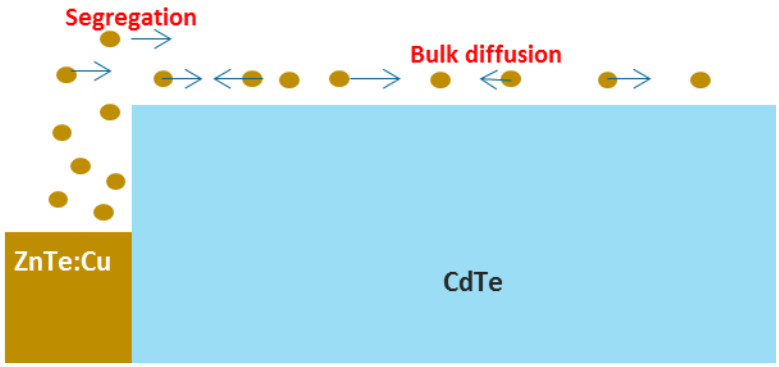

Figure 4.8. Schematic illustration of Cu migration from the source layer into CdTe material.

4.3.2 Simulation Scheme for Cu Anneal Process

In the experiment, following the deposition of Cu source layer, the samples (can be sx-CdTe wafer or px-CdTe solar cells) are annealed at high temperature (usually varied between 150 ^{o}C to 300 ^{o}C) for certain durations (usually less than 30 minutes) [1], [51]. For this particular study, ZnTe:Cu/sx-CdTe samples were annealed at 250, 300 and 300 °C for 40, 20 and 12 minutes, respectively [47]. And for the px-CdTe solar cells fabricated at Colorado State University, anneal was conducted around 200 ^{o}C for 200 seconds [9].

Most importantly, both sx-CdTe samples and px-CdTe cells are commonly measured at room temperature. Thus, measurement performed with these samples, including ToF-SIMS and IV-characteristics, is not only determined by annealing condition, but also affected by cooling process. The cooling effect also has crucial importance in terms

of solar cell characterization [34], [58]. Hence simulating cooling process also has crucial importance in terms of comparing simulation results with experiments.

Given this, simulation of temperature changes is performed before we make any comparison to experimental results. During each annealing simulation (also stress cases), several transient of the simulations will be extracted for the later cooling process. For example, in the annealing case, as four different annealing durations were applied in experiments, defect distribution (and potentials) at the corresponding time step will be extracted. By doing this, we could get four initial profiles for the cooling simulations in one annealing simulation. Usually it takes about 10 – 15 minutes for the annealed samples to cool down to RT from typical annealing temperature of 200 – 300^{o}C.

4.3.3 Predictive Simulation of Device Performance Changes

As the primary target in this work is defect migration caused by device performance changes, the initial condition of defect distribution is of crucial importance. The most reliable procedure is to perform long term stress simulations on top of the aforementioned annealing simulations: using pre-simulated annealed and cool-downed defect profile as the initial condition. Doing this, avoids oscillations or divergence caused by un-equilibrium initial guess of defect profiles at the beginning of simulations. More importantly, pre-simulated defect profile probably is the best initial guess of defect distribution in fabricated solar cells. However, such statement can only be made with true confidence in employed defect chemistry and annealing simulation results.

Similarly to the annealing process, temperature change is commonly present in stress test for solar devices. Many publications claimed that device performance is

measured at room temperature, commonly referred to as ex-situ measurement under STC, regardless of the stress conditions [9], [59]. In these cases, people are usually interested in the long-term degradation of the device. On the contrary, many also reported continuous device measurement conducted during the stress without temperature changes [60], i.e in-situ measurement. Such arrangement is commonly employed to avoid uncertainties of the ex-situ measurement introduced in the cooling process, which is also a part of device's stress history, especially for solar cells with fast transient behaviors at room temperature. Given the fact that temperature changes may or may not be presented in these stress experiments, corresponding simulations need to accommodate such experiment setup for meaningful comparisons between them.

4.3.4 Tracking of Bias Condition in Predictive Simulations

As the most common operation mode of photovoltaic devices in their applications, Maximum Power Point Tracking is a typical bias condition employed in reliability studies of solar cells. Open-circuit is another usual bias condition in these investigations, especially when MPP tracking is not available or limited. Although fixed voltage bias could be employed to mimic the ever changing Vmp or Voc condition in simulations, larger performance changes occurring during these tests could easily challenge this assumption. Furthermore, as a self-consistent system, simply set fixed voltage bias condition my results in solutions far from the true equilibrium states between device operation and point defect evolution. Thus, tracking of bias conditions is essential to eliminate potential errors come from fixed voltage bias conditions.

Due to the unique integration of device simulations in this developed solver, realization of bias condition tracking is straight forward. I-V simulation utilizing real-time dopants profiles, are frequently performed in simulations that require bias condition tracking. Vmp or Voc extracted from the simulated I-V characteristics is applied to the steady states simulation in the next time step to reflect changing in bias conditions, electrostatic potential and carrier distributions. Figure 4.9 schematically illustrates the flow chart of the integrated solver with bias condition tracking.

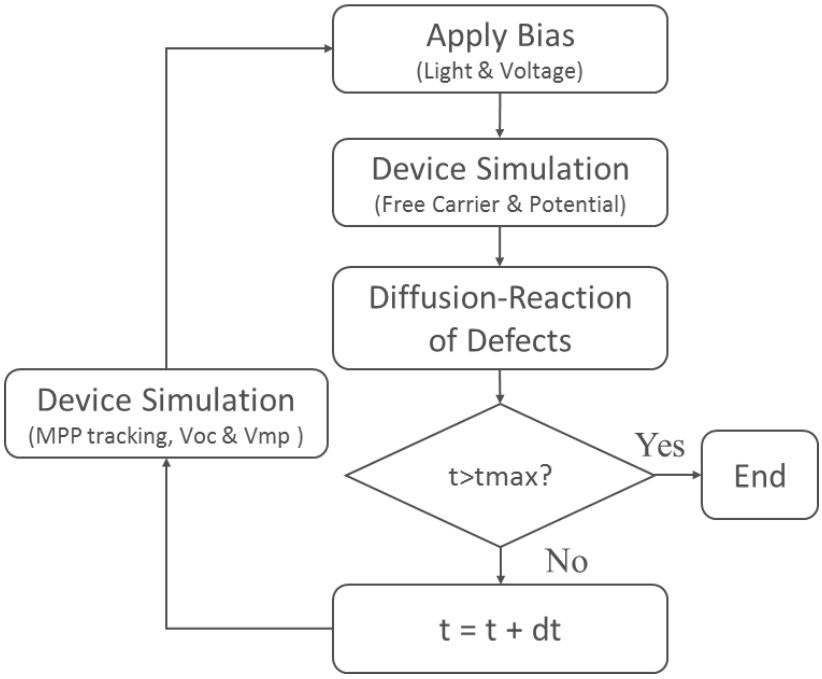

Figure 4.9. Flow chart of simulations with bias condition tracking.

In comparison to the flow chart in Figure 4.3, Apply Bias block is now included in the coupling loop to allow bias conditions. Also, free carrier and electrostatic potential update is performed prior to the diffusion-reaction process of point defects, so that updated bias condition could impact defect migration immediately. However, it is important to note

that frequent I-V simulations could significantly increase computational burden of the solver, thus it is only invoked when needed.

4.3.5 Time-Dependent IV Simulation with Active Defects

Another unique scheme provided by this self-consistent simulator is time-dependent IV simulations with active defects. In this scheme, we are interested in active defects impact on direct IV measurement. As it is well known in the photovoltaic research community, IV characteristic with similar conditions could result in complete different IV-curves from the same device based on the direction of voltage sweep or even sweeping frequencies, especially in Perovskite and thin-film technologies. Many have accredited such behavior to mobile ions' presence in these devices [61], thus it could be considered as short-term metastability as well. Since the developed solver already integrates defect migration with steady-states device simulation, mobile ions migration during IV measurement could be investigated using this unified solver.

The standard procedure for such I-V simulation utilizes the solution of device simulation performed at each time stamp, with sweeping voltage bias in a certain direction and frequency. Corresponding defect evolution is again, determined by the diffusion-reaction part, with continuously updated potential and carrier distributions from the steady-state device simulation. Figure 4.10 below shows typical current output as a function of time evolution in this type of simulations. Current density spikes are commonly observed at the beginning of new voltage steps, suggesting a certain amount of time stamps inside each voltage step is required to achieve stabilization or equilibrium for the given voltage bias conditions.

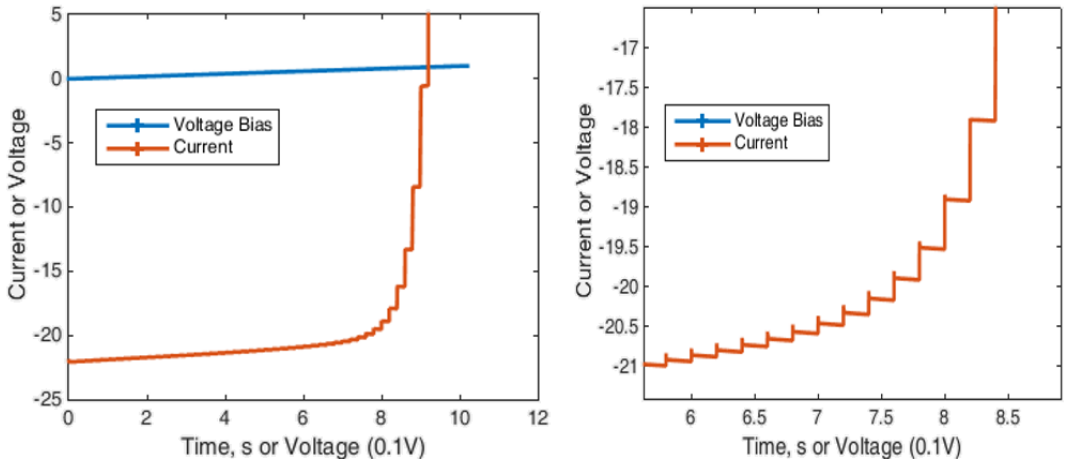

Figure 4.10. Typical voltage bias and current output plotted against time evolution in time-dependent I-V simulations. 0.1V/s sweeping rate is employed.

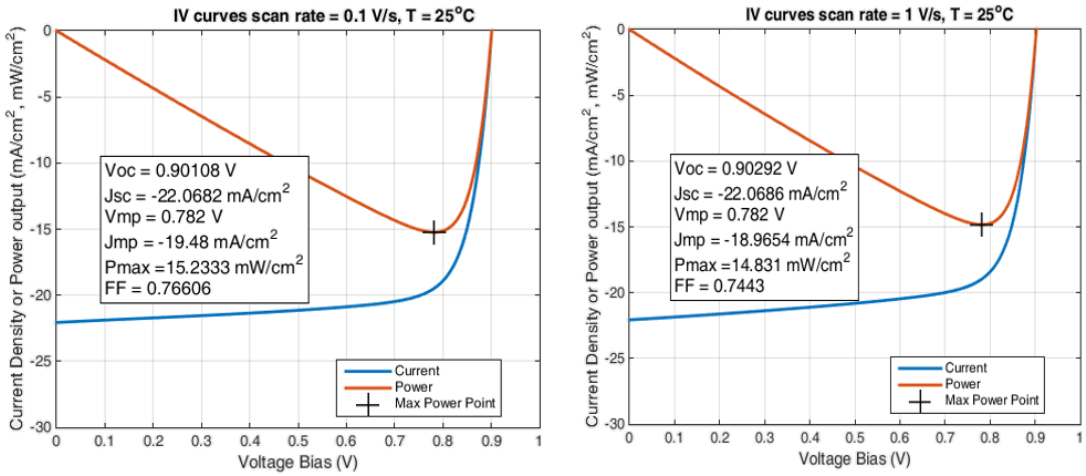

Figure 4.11. Comparison of IV-characteristics simulated by different sweeping rate.

Figure 4.11 compares two time-dependent I-V simulations with different sweeping rate. Based on the simplified Cu-only defect model, reducing sweeping rate from 1V/s to 0.1V/s, raised the fill factor hence overall efficiency of the solar cell, by about 3%. Such enhancement most likely is caused by more uniform doping profiles achieved through slow migration of $Cu_i(+)$ towards junction area, or gradual passivation of acceptor centers in the depletion region. Such behavior of CdTe thin-film devices has not been reported previously.

CHAPTER 5

SIMULATION RESULTS

In the rest of this thesis, we discuss the agreement and discrepancy achieved between simulation and experiments on Cu migration in CdTe.

5.1 COPPER ANNEAL IN SX-CDTE

An experimental study of Cu migration in single crystal CdTe was done at First Solar Inc. (Perrysburg, OH). In this experiment, thin Cu-containing ZnTe (ZnTe:Cu) layers were deposited on highly-resistive sx-CdTe substrates provided by JX Nippon. We did not apply any additional treatment that could affect the compensation of sx-CdTe before ZnTe:Cu deposition, thus the concentration of intrinsic defects, especially Cadmium Vacancy (V_{Cd}), should be negligible. The target concentration of Cu in the ZnTe:Cu layer was set as 4×10^{20} cm^{-3}. Later experiments suggest that the Cu concentration is around 6×10^{19} cm^{-3} in the ZnTe layer, which is significantly lower than the original target value. Such difference could be caused by low resolution and broadening effects of the SIMS technique. Diffusion anneals were performed at 250 ˚C, 300 ˚C and 350 ˚C for four different durations at each temperature value. The atomic Cu depth profiles were measured in every sample using ToF-SIMS. The detection limit of such technique is around 10^{16} cm^{-3} (marked as the control sample without annealing process in Figure 5.1). Alongside, ten measured profiles corresponding to different annealing recipes are also shown in Fig. 5.1. The Cu profile for the sample annealed at 350 ˚C for 9 minutes lies close to the profile for the 12 minutes case, and is also not presented for a better view of the others. It is important to note that the ToF-SIMS measurements were conducted at room temperature after a natural

cooling process of the samples. The high concentration of Cu appearing in the first 0.5 µm is the residual Cu concentration from the ZnTe layer. Focusing on Cu in CdTe, we see that Cu penetrates deeper into the CdTe as we increase the annealing time or the annealing temperature. In samples that were exposed to higher annealing temperature (350 ˚C samples) or longer duration of the annealing process (300 ˚C for 20 minutes sample), abnormally high concentration of Cu (>10^{18} cm^{-3}) is observed in the first 0.5 µm of CdTe (0.5<x<1 µm region). This could be explained by the broadening of ZnTe or formation of ZnCdTe, caused by Zn diffusion at similar annealing temperature with shorter annealing time [51], [52]. However, such behavior is beyond the scope of this paper as Cu in bulk CdTe is the primary focus of this work. Another important finding in this experiment is that the peak of the Cu concentration in the CdTe layer is 1 to 2 µm beneath the interface. This is probably caused by the back diffusion of Cu during the cool down process and will be addressed later in this section.

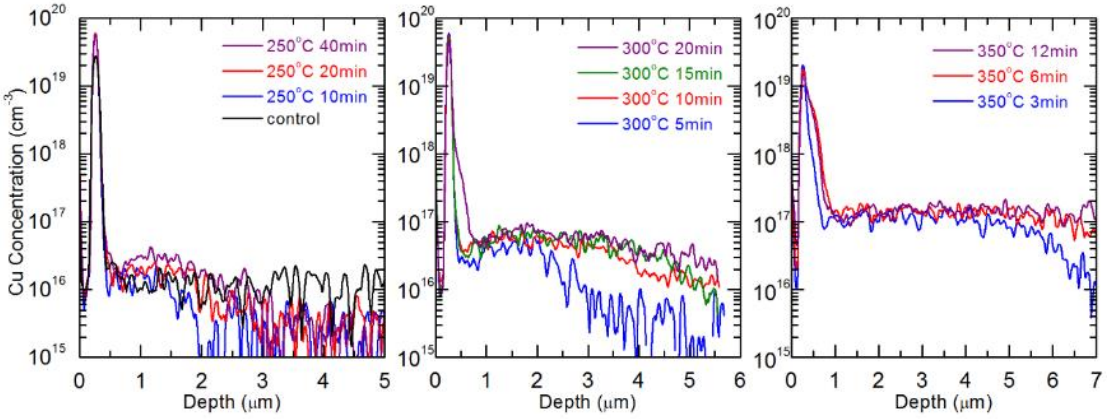

Figure 5.1. Atomic Cu profiles achieved with different annealing recipes. Black pentagrams represent the control sample without any annealing.

For the simulation part, a high concentration (5×10^{20} cm^{-3}) of Cu_i was assumed in the 0.5 μm thin ZnTe:Cu source layer. This simulated initial Cu concentration is larger than the actual measurement and the original target value. Using larger formation energy of Cu in ZnTe layer, the equivalent of larger segregation factor across the interface, will eliminate the effect of higher Cu source concentration. In particular, a 0.45 eV difference in the standard formation energy of Cu_i was employed to achieve the proper Cu concentration in CdTe substrate with different annealing recipe in simulation. A constant 10^{17} cm^{-3} p-type doping was maintained in this layer during the entire simulation. This assumption is consistent with the literature [51]. The thickness of the CdTe bulk was set as 15 μm to avoid reflection of defects from the end of the CdTe "wafer". Negligible amounts (10^{13} cm^{-3}) of V_{Cd} was initialized in the samples prior to the annealing simulation. Neumann boundary conditions were applied for both ends of the simulation domain to maintain conservation of all defects. In order to obtain the electric field properly, widely accepted carrier transport properties and material properties of px-CdTe and ZnTe were employed in the simulations. Although better carrier lifetime and material quality should be expected in sx-CdTe, their impact on the Cu profiles in sx-CdTe remained unclear. Nevertheless, there may be no considerable impact since no (or negligible) electric current flows through the samples during the annealing process.

Using first principles parameters [21], [25], [26], the fitted diffusivities and ionization energies shown in Table 5.1, good agreement between experiment and simulation was achieved for the annealing process with different temperatures by the same set of diffusion-reaction parameters. The solid lines in Figure 5.2 represent the simulated Cu profile with each annealing recipe. As listed in Table 5.1, the fitted diffusion barrier

energy of both interstitials were 0.26 eV larger than the DFT value. Such difference may come from the implementation of incomplete physical models in this work, which will be addressed later in this section. Although the back diffusion of Cu during cool down can be qualitatively simulated, some temperature dependency is present: the higher annealing temperature, the larger Cu depletion is achieved near the interface, which will be discussed later in this section. We also need to point out that the room temperature hole concentration in the saturated region of CdTe, as a result of both partial ionization and compensation of Cu dopants, crucially depends on this ionization energy of Cu_{Cd} listed in Table 5.1. By using a slightly higher (0.25 eV) ionization energy of Cu_{Cd} acceptors, the free hole concentration is maintained below 3×10^{15} cm^{-3} in all "samples" at room temperature.

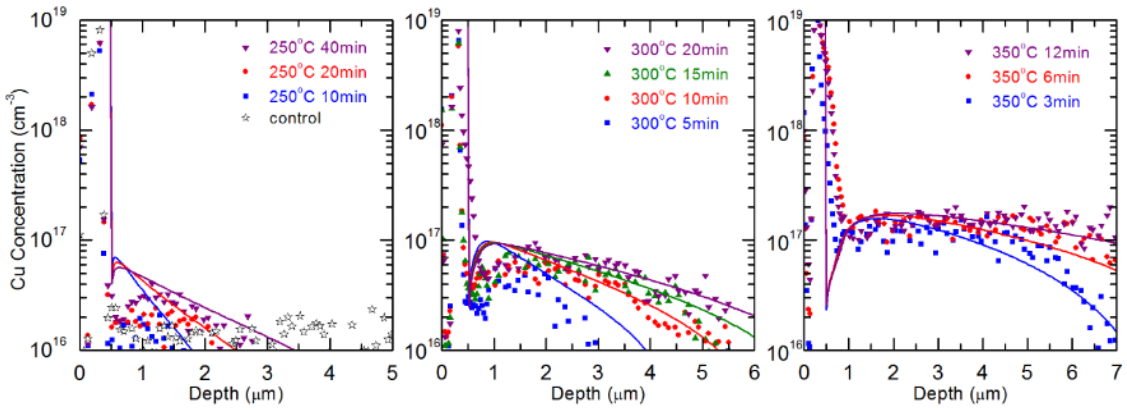

Figure. 5.2. Atomic Cu profiles achieved with different annealing recipes. Black pentagrams represent the control sample without any annealing. Solid lines represent the simulated Cu profiles after cooling to room temperature.

Table 5.1 List of Employed Parameters and Theoretical Values

Defect	D_0 (cm^2/s)	E_D (eV) [a]	ε (eV) [b]
$Cu_i(+)$	4.9×10^{-3}	0.718	1.37
(DFT value)	(6.3×10^{-3})	(0.46)	(1.36)
$Cu_{Cd}(-)$	-	-	0.25
	-	-	(0.22)
$Cd_i(2+)$	3×10^{-4}	0.727	1.3
	(3.21×10^{-3})	(0.47)	(1.29)
$V_{Cd}(2-)$	-	-	0.36
	-	-	(0.36)

[a] E_D here is the energy of the diffusion barriers illustrated in Fig. 2.
[b] ε is the defect transition energy level (ionization energy) with respect to the valence band minimum.

Figure 5.3 depicts the simulated defect distribution and band diagram of the sample right after a 3 minute 350 ˚C annealing process (corresponding to the blue squares and blue line in Figure 5.2, but without cooling process), which explains the saturation behavior of Cu in CdTe. The original built-in electric field between highly p-type doped ZnTe and highly-intrinsic CdTe limits $Cu_i(+)$ from moving into the CdTe region. However, a small amount of Cu_i is able to diffuse into CdTe. Therefore, $Cu_i(+)$ quickly knocks Cd atoms off, generates immobile $Cu_{Cd}(-)$ and mobile $Cd_i(2+)$ under the backward reaction of Reaction 1 listed in Table 3.1. As part of $Cd_i(2+)$ being drifted into the ZnTe layer under the same built-in electric field across the interface, normally known as out diffusion, the p-type region starts to form in CdTe. It is important to note that since charge is conserved in all reactions, achieving p-type doping without $Cd_i(2+)$ moving out of CdTe is very difficult. As Cu forms acceptors in CdTe, an electric field is generated between the Cu occupied p-type region and the intrinsic CdTe region without Cu, which again prevents further movement of Cu_i into the intrinsic region of CdTe. Once the distribution of defects gets close to the balance of all involved reactions, such as $0.5<x<6$ μm region in Figure 5.3,

less Cu_{Cd} will be generated. Hence more Cu_i can travel through this saturated region to occupy Cd sites in the newly formed p-i junction area (x>6 μm in Fig. 4). The line with diamonds (green in the online version) in Figure 5.3, labeled as "Free Holes", demonstrates the distribution of free holes in the simulated sample. This indicates that partial compensation between Cu_{Cd}(-) and Cd_i(2+) is achieved at 350 ˚C as the atomic Cu concentration is around 2×10^{17} cm^{-3} while the holes concentration is about 4×10^{16} cm^{-3}. However, partial ionization of the Cu_{Cd} acceptors plays a minor role in the compensation mechanism since the acceptor level of Cu_{Cd} is not that shallow. About 90% of Cu_{Cd} acceptors in the saturated area are ionized at 350 ˚C according to detailed results from our simulation.

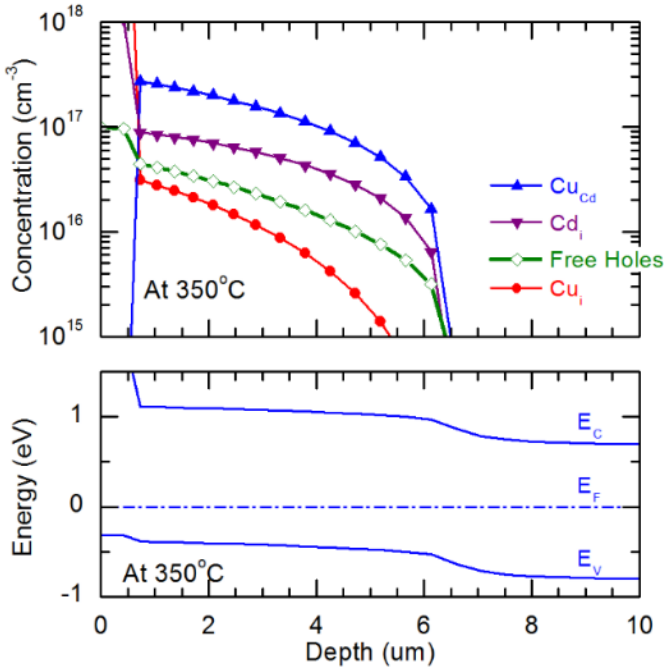

Figure 5.3. Simulated profiles of major Cu-related defects and free carriers (top panel) and band diagram in the ZnTe:Cu/sx-CdTe structure after 3 minutes of annealing at 350 °C (bottom panel).

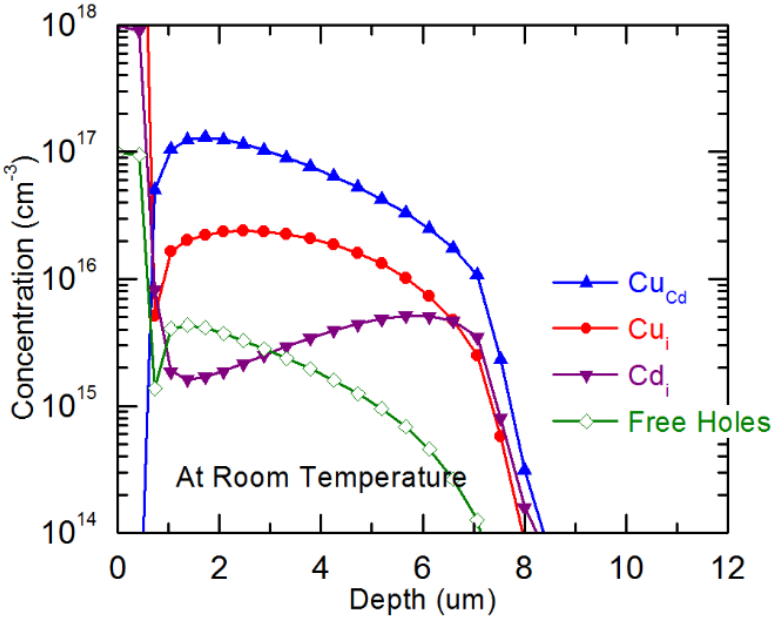

Figure 5.4. Simulated profiles of major Cu-related defects in the sample after 3 minutes annealing at 350 ^{o}C and an extra 12 minute cooling process. Simulated Cadmium Vacancies are neglected as the maximum concentration is below 10^{13} cm^{-3}.

As we cool down the sample to room temperature with a natural decay of the ambient temperature (corresponding to the blue squares and blue line in Fig. 5.2), the Cu depletion near the interface is simulated as indicated in Figure 5.4. In general, as the temperature decreases, Cu_i starts to diffuse back into ZnTe due to the 0.45 eV difference in the standard formation energies of Cu_i between CdTe and ZnTe, which triggers the dissociation of Cu_{Cd} (forward reaction of Reaction 1 listed in Table 3.1). As the dissociation consumes most of the Cd_i, Cd_i stored in ZnTe starts to diffuse back into CdTe. Once these Cd_i reach the reaction-unbalanced CdTe, they continue to dissociate Cu_{Cd} to reach a new equilibrium among involved reactions. Since only the interface region can get supplemental Cd_i, the Cu reduction is more obvious near the interface. As the temperature

further decreases, both the reaction and diffusion rates become quite slow. Still, this progress should not be completely stopped right after the cooling process. Experimental evidence of Cu movements in CdTe devices stressed at 65ºC has been reported recently [9].

This back-diffusion mechanism could also explain Cu depletion's temperature dependency in simulations presented in Fig 5.2. First of all, the back-diffusion mechanism itself can be seen as the natural progress of Cu approaching the lower solubility limit during the cool down process. Thus, larger difference of Cu concentrations between the interface and bulk is presented in simulations with higher annealing temperature. Additionally, the simulated Cu concentration is around 4×10^{16} cm^{-3} near the interface after cool-down, regardless of the annealing temperature (see Fig. 5.2). This does not necessarily denote the Cu solubility limit in CdTe at RT, but in some degree represents the Cu solubility at certain temperature that diffusion-reaction progress of Cu becomes too slow in our simulations. As detailed simulation result suggests, this temperature is in the range of 140 – 160 ˚C. Moreover, the simulated Cu depletion heavily relies on the diffusion coefficients of Cu_i and Cd_i, as the former one diffuses back into ZnTe:Cu while the latter one diffuses in the opposite direction. Higher diffusivity allows more interstitial atoms to move across the interface, thus triggering more dissociation reaction of Cu_{Cd} at high temperature in general. As a larger diffusion barrier energy was employed for both of them, such dependency is further enhanced due to the larger variance in the diffusion coefficients of both interstitial atoms. Also, considering the fact that Cu depletion is clearly present in the 250 ˚C anneal experiments but not that well in the corresponding simulations, we believe that the

diffusion coefficients used in this case, give good agreement between Cu profiles obtained from simulations and experiments, have larger temperature dependency. By including donor-acceptor centers, (such as Cd_i-Cu_{Cd} and Cu_i-Cu_{Cd} complexes) into the simulator, smaller diffusion barrier energy of both Cu_i and Cd_i can be employed to achieve good agreement with experimental Cu profiles. Detailed analysis of this augmented model will be published soon [62].

Figure 5.4 also shows that the free carrier concentration drops below 3×10^{15} cm^{-3} level with only a smaller reduction in atomic concentration of Cu at room temperature. More importantly, the new compensation is mostly achieved between Cu_{Cd}(-) and Cu_i(+). Therefore, during cooling, the compensation mechanism is changed. The observed change is a complex process determined by diffusion, drift, reactions, and temperature-dependent Fermi-Dirac statistics both for free carriers and Cu_{Cd} acceptors. Again, the resulting room temperature hole density depends crucially not only on donor-acceptor compensation but also on the possibility of the ionization of Cu_{Cd} acceptors: In average, only 30% of Cu_{Cd} is activated as acceptors in the saturation region of this particular "sample". If larger dopant activation energy was employed in our simulation, the ionization could be even weaker. For example, replacing this 0.25 eV ionization energy of Cu_{Cd} acceptors by 0.22 and 0.28 eV, the resulting room temperature average hole concentration is 5.4×10^{15} and 1.3×10^{15} cm^{-3}, respectively. The recent development of low-temperature time-resolved photoluminescence shows a strong potential to estimate the ionization energy and concentration of Cu_{Cd} acceptors [30], [63], which could further help us on understanding the limited incorporation and self-compensation of Cu doping in CdTe.

5.2 COPPER ANNEAL IN PX-CDTE DEVICES

Experimental study of Cu diffusion in px-CdTe solar cells was done at Colorado State University (CSU). In this experiment, CdTe solar cells were fabricated using CSU's standard close-space-sublimation process. CuCl treatment (performed at 160^{o}C, 180^{o}C and 210^{o}C to control the amount of Cu that is diffused into CdTe) followed by an annealing at 200^{o}C were performed after a standard 400^{o}C 3 minutes $CdCl_2$ treatment. Once the entire fabrication process was finished, ToF-SIMS measurement, IV-characterization and CV characterization were performed at room temperature. Details of the experiments can be found in [9]. Simulations with the same temperatures were performed in order to get proper defect properties and initial Cu distributions in the devices. There are three major differences between our simulations and the real devices: (1) no grain-boundary in our 1D simulation, (2) Cu-containing ZnTe layer simulated as Cu source instead of CuCl, due to the lack of CuCl parameters and (3) Cl-related defects (such Cl_i, Cl_{Te} and Cl_{Te}-V_{Cd}) were neglected in the simulations.

Figure 5.5 compares the simulated Cu profile and the SIMS measured profile. It is clear that the atomic Cu profile were matched by our simulation qualitatively, while the simulated carrier densities were slightly lower than the measured data. Many possible reasons could be related to such discrepancy: it could be an inaccurate defect transition energy level which increases the possibilities of acceptors being ionized. Or a non-realistic defect chemistry that does not represent the real compensation mechanisms which were assumed in the simulations. Another possibility here is the Cl-related defects missing in the theoretical model. The atomic concentration of Cl is expected to be 10^{18} cm^{-3} in thin-

film CdTe absorber [64], [65]. Cl defects compensate each other as the carrier concentration in Cl treated CdTe thin-films are usually highly intrinsic [2]. Contrary to the experimental data, the simulated free carrier density shows some dependency on the Cu concentration, which is also an indication that the compensation mechanisms in CdTe are not completely understood.

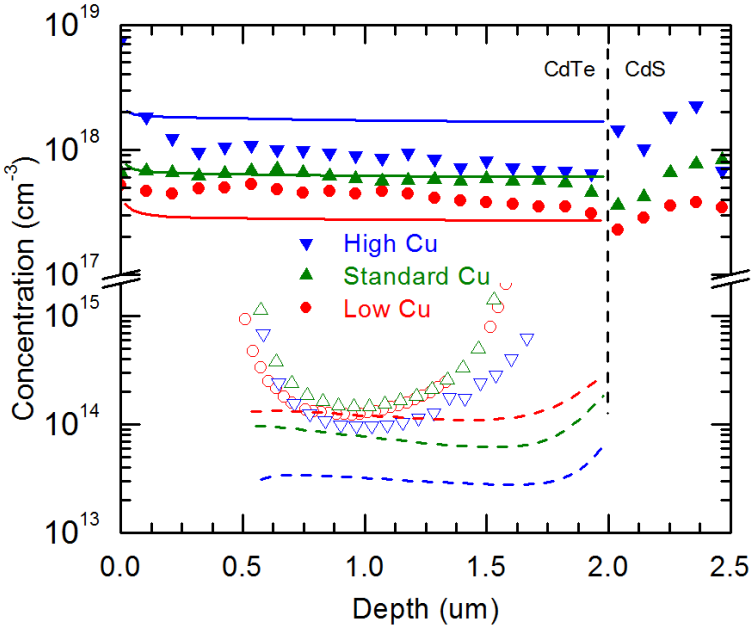

Figure 5.5. Comparison of simulated (lines) and measured Cu profiles (solid marbles) and carrier density (open marbles) in CdTe solar cells with the same annealing recipe.

Applying the more advanced Cu-Cl interactions listed in section 3.3, simulation can be used to predict the detailed distribution of defects in px-CdTe solar cells. Figure 5.6 depicts the distribution of 17 Cu-Cl defects in CdTe absorber layer at room temperature after a 10 minutes 300ºC annealing. The total Cu concentration plotted by the black dash line is maintained above $10^{17}cm^{-3}$ through the entire absorber layer, this particular number, although is not in agreement with CSU's device, is indeed consistent with other reports

[27], [51]. Also, in agreement with most reported Cu distribution measurements, a higher Cu concentration is present near the back contact and front junction in these new simulations with Cu-Cl defects. The bumps near the back is partially due to the source layer and diffusion process while the front bump is directly related to the depletion of positively charged ions in a p-type depletion region. Better agreement between the Tof-SIMS measured total Cu profiles from the CSU device could be achieved with further investigation of the parameters of the Cu density or the segregation factor in the source layer.

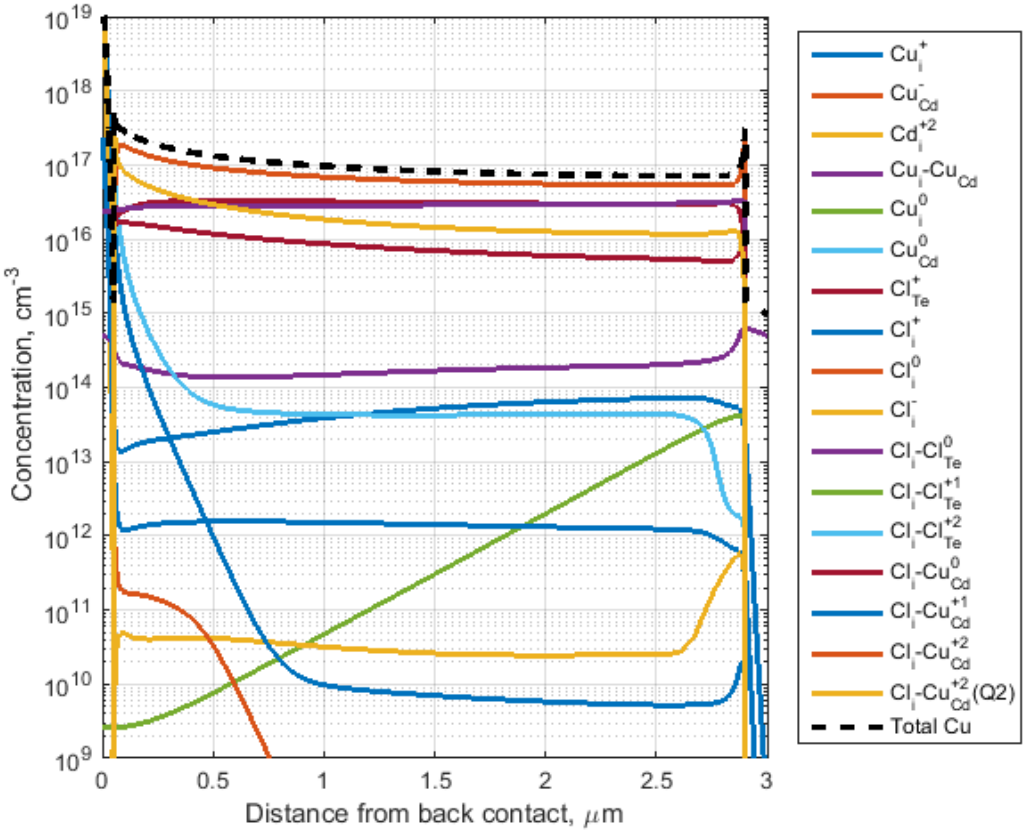

Figure 5.6. Detailed distribution of 17 common Cu-Cl defects achieved in annealing simulation.

5.3 PREDICTIVE SIMULATION OF LONG TERM DEVICE PERFORMANCE

A different set of cells were fabricated with the same settings but thicker (2.5 um) CdTe layer. Once the entire fabrication and initial characterization are finished, all cells were stressed at 65^{o}C under illumination of ~1 sun (1kW/m^{2}) for a total time of 831 hours. One set of the cells were stressed at Short-Circuit (SC) conditions while another were exposed to Open-Circuit (OC) stress. Device characterization was performed several times during that time span. Inspection of the Cu concentration profiles (Figure 5.7) shows that OC-stress seems to not move Cu atoms away as the profile is close to the pre-stress curve. On the contrary, SC-stressed device has a reduced Cu concentration. Most likely the reduction is attributed to the migration of positively charged Cu ions towards the back of the device due to the electric field within the SC conditions of the device. Contrary to the changes in atomic Cu concentrations, carrier densities remain the same for SC-stressed device but increases 100% in the OC-stress experiments.

Simulation results show a similar Cu depletion in CdTe layer for SC-stress (Figure 5.7): 15% of total Cu was reduced during the SC-stress simulation in 100 hours, which is slightly faster than the experimental observation that Cu concentration reduces 60% in 831 hours. Smaller Cu depletion (7% of total Cu) is also presented for the OC-stress in our simulations. Most likely, both depletion is caused by the $Cu_i(+)$ back diffusion due to the ZnTe:Cu source layer, while there is no such layer (hence no or less back diffusion of Cu_i) in the experimental setup. The fact that SC-stress depletion is faster could be related to the strong electric field existed in the junction area under SC conditions where such electric field should be significantly weaker under OC conditions. If the back diffusion of Cui could

be reduced or eliminated, by alternating the source layer or changing the formation energy of Cu_i in the source layer, our simulations could provide better understanding of the hypothesis that built-in electric field of CdTe solar cells is the main reason for the Cu depletion observed in SC-stress.

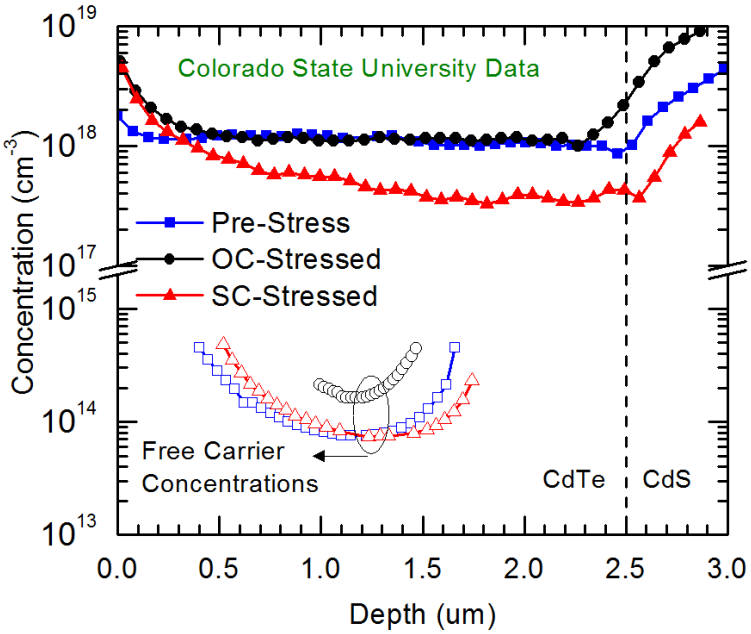

Figure 5.7. Comparison of SIMS measured profiles of Cu concentration (solid marbles) and carrier densities (open marbles) for pre-stress, OC-stress and SC-stress.

Figure 5.8 compares the detailed defect distribution before and after both type of stresses, showing that the dissociation of Cu_{Cd} acceptor is the main reason for the p-type peak near the junction area. Built-in electric field of the device pushes Cu_i from the depletion region towards the back contact. Due to the missing of Cu_i, quasi-equilibrium of the defect chemistry breaks down, Cu_{Cd} starts to dissociate. The built-in potential in the depletion region once again pushes newly released Cu_i away, results in further dissociation of the Cu_{Cd} acceptors near the junction area. Due to the increase of p-doping near the

interface, depletion region width shrinks, which actually allows more Cu_i to move towards the main junction. However, such movement reflects only the changes of electric field in that specific area, but not implications of the actual movements of total Cu atoms. Due to the weaker electric field in OC condition, less Cu_i could be pushed away from the junction area, the dissociation of the Cu_{Cd} acceptors is significantly weaker.

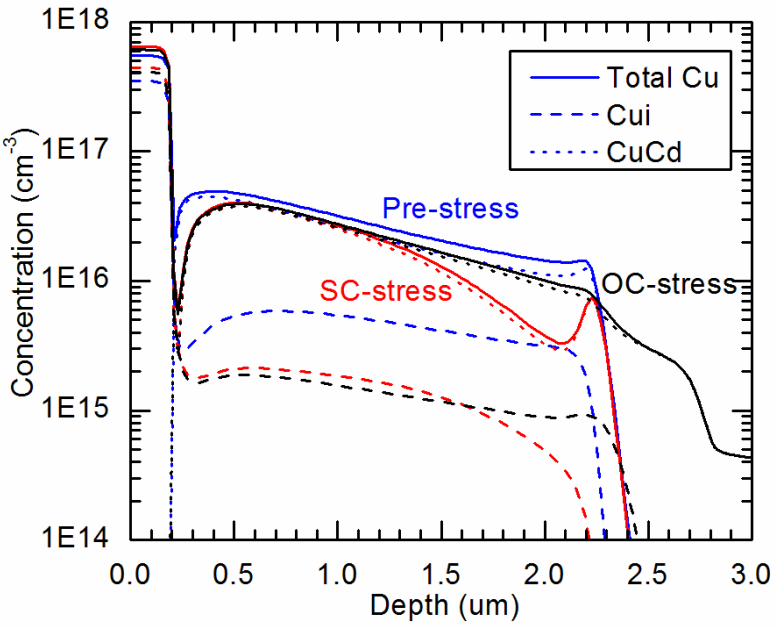

Figure 5.8. Comparison of simulated Cu defect profiles (solid lines) for pre-stress, OC-stress and SC-stress devices.

Correspnding carrier density for the stressed devices are illustrated in Figure 5.9 as well. OC-stress conditions increase the holes density in the absorber layer and decrease it near the junction, which conceivably is caused by Cu_i penetration deeper in the device, results in more uniformed distribution of free carriers. On the contrary, SC-stress pushes mobile Cui(+) donor away from the right (front) of the device, which implies Cu_i back diffusion accelerated by the electric fields, causing low acceptor in the bulk but high

acceptor density near the junction area. It is important to note that the carrier density peak between 2 um to 2.5 um for the SC-stressed device (see red dash line in Figure 5.7), is the major cause of the Fill-Factor (FF) reduction in our simulations. However, such phenomena cannot be observed from the general CV measurement since it is usually employed to characterize the mean carrier density in the thin film but not the detailed distribution of carriers in the entire thin-film, let alone the fact that measured carrier density in the depletion region is always neglected in these measurements.

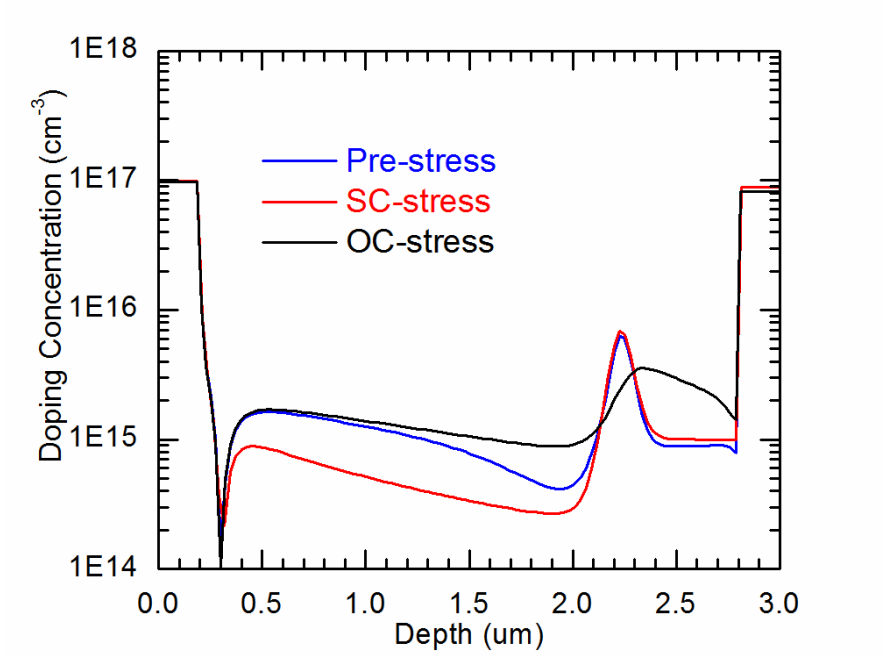

Figure 5.9. Comparison of simulated net acceptor distributions in CdTe solar cells for pre-stress, SC-stress and OC-stress.

Corresponding device performance in these stress simulations are presented with the experimental data in Figure 5.10. The simulation results agree qualitatively with the experiments as FF contributes to the majority of the device performance degradation while both J_{SC} and V_{OC} are stable over that time span. The simulated device degradation is 10

times faster than the experiments most probably due to inaccurate diffusion-reaction parameters employed to simulate Cu's migration or the Cu_i back diffusion caused by ZnTe:Cu layer that has been discussed in this report. The increasing trend of Voc and the gradual redeuction in Jsc in simulation mostlikely are caused by the increasing of p-type dopants in the junction area.

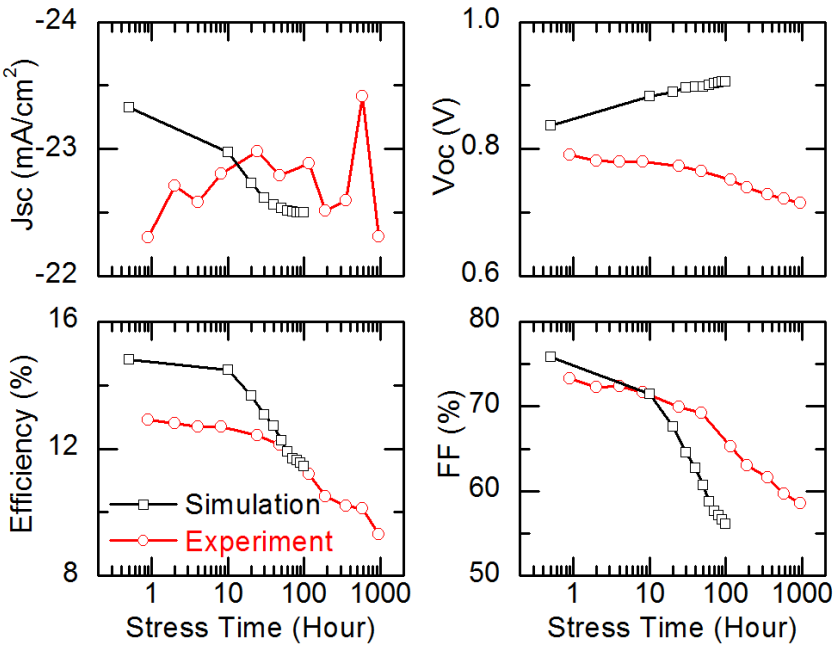

Figure 5.10. Comparison of simulated defect distributions in CdTe solar cells for pre-stress and SC-stress.

It is important to note that during these stress simulations, constant carrier lifetime (equal to 3 ns) and constant mobility of carriers were assumed in the theoretical model. The presented device degradation is purely caused by the variation of the doping profile in the device. However, in real experiments, both of them are expected to change during the stress test. Kuciauskas *et al*. reported Cu_{Cd} as the main recombination center in CdTe [15], addressing that carrier lifetime should be calculated precisely in the simulations when

massive Cu migration occurs. The inclusion of dopant dependent lifetime and mobility is currently being implemented within our group.

Another possible mechanism that has not been accounted for is the carrier-defects interactions. Although steady-state ionization status of each defect is calculated based on distribution of carriers (quasi-Fermi level of electrons and holes), the transient of such ionization process is not being modeled, as the ionization reaction rates (nanosecond SRH recombination lifetime of carriers) were considered to be orders of magnitude faster than the defects migration. However, such assumption may not be completely valid. Similar fast transient behavior was observed in px-CdTe solar cells fabricated at both National Renewable Energy Laboratory (NREL) [66] and CSU. Since the metastable behavior was observed within hours of stress at room temperature, massive migration of Cu defects probably was not achieved in those solar cells, indicating that such phenomena are not caused by the fast movement of dopants in our simulations, but are related to the gradual passivation/activation processes of recombination centers commonly presented in CdTe thin films. We are also working on simulations of such ionization reactions for further investigation of metastable behaviors observed in CdTe thin-film solar cells.

5.4 PREDICTIVE SIMULATION OF SHORT TERM METASTABILITIES

The following experiment was performed to further understanding the light soaking effect commonly observed from CdTe solar cells: four “CSU” CdTe solar cells with Te/Ni back contact [67] were dark soaked at 60°C for up to 17 hours. Afterwards, two samples were light soaked at the same temperature with AM1.5 solar irradiance, while the other two samples were kept in dark at 60°C. In both groups, one device was short-circuited and

the other one was forward-biased: open-circuited in the light soaking group or 0.7V forward-biased in the dark group. In the biased case, smaller internal field is expected, comparing to the short-circuited cells. Several in-situ light J-V measurement were performed for each cells during these soaking experiments at the same stress temperature of 60°C. Hence, temperature-dependent behvior of solar cells is avoided in this study.

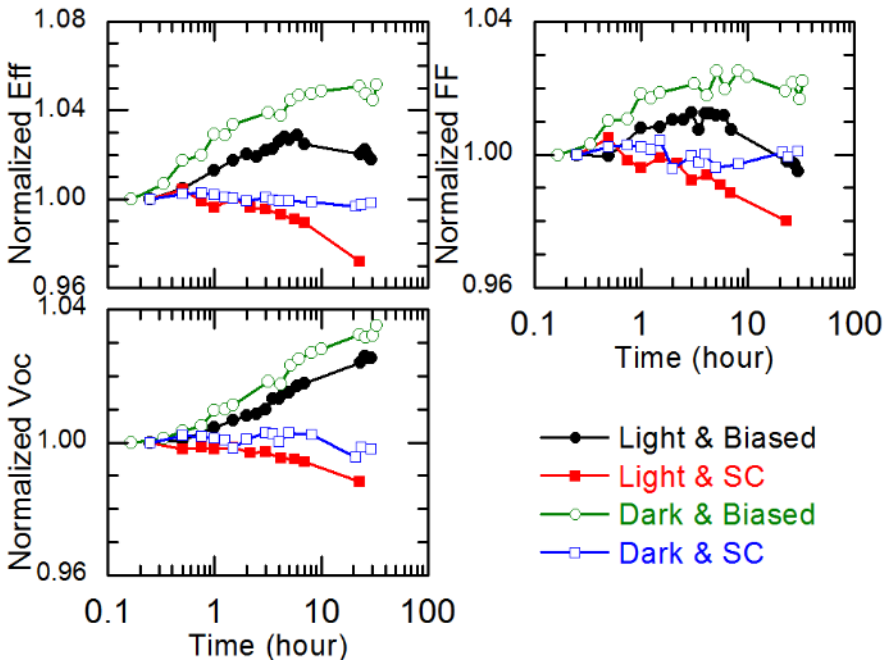

Figure 5.11. Device performance under different soaking conditions. In-situ IV characterization performed at stress temperature (60°C), thus avoid potential transients could occur before STC test.

Figure 5.11 shows the changes in device performance of all four devices as a function of time, under different light and voltage bias conditions as indicated. It is clear that performance enhancement is presented in both forward-biased devices (marbles), regardless of the light conditions. On the other hand, no significant increment were

observed in both short-circuited devices (squares). However, steady decrease in efficiency and fill factors were presented in the short-circuited and light-soaked device (red solid squares), which could be an indication of commonly observed light-induced degradation in CdTe solar cells [68], [69]. Stable performance was observed in the short-circuited device under dark soaking (blue open squares), as neither light nor voltage bias was applied to it. No significant changes were presented in J_{SC} of all devices thus they are neglected in this discussion. Between the forward-biased (performance enhanced) solar cells, V_{OC} curves share similar path, which might suggest that the V_{OC} growth is caused by the reduced internal field in these devices. However, the FF curves do not follow with each other: gradual increase was presented in the dark soaked device (green open marbles) with minor fluctuations after 10 hour of stress while an initial increment followed by steady reduction was observed in the Light & Biased cell (black solid marbles). Since the other light-soaked but short-circuited cell (red solid squares) shows similar degradation of FF, especially after 6 hour of light soaking, it is highly possible that the drop in FF is related to light soaking itself. Such reduction in FF also limited the efficiency growth of the Light & Biased device. In summary, experiment shows that light soaking (light-generated excess carrier) decreases FF hence overall device performance while forward-bias helped to boost V_{OC}, FF and overall conversion efficiency.

From simulation side, a standard ZnTe/CdTe/CdS structure is employed with simplified dopant compensation picture. Namely, 10^{16} cm^{-3} Cu_{Cd}(-), 0.4×10^{16} cm^{-3} Cu_i(+) and 0.5×10^{16} cm^{-3} background donor concentration are uniformly distributed in CdTe as the initial defect distribution, resulting in 10^{15} cm^{-3} hole density in the CdTe absorber layer.

Since solar cells were dark soaked for 17 hours prior to any soaking experiment, we first simulate the equilibrium of the defect system in CdTe cells under dark without any voltage applied. Figure 5.12 shows the equilibrium distribution of Cu dopants as well as the band diagram of the solar cell under dark at 60^{o}C. Due to built-in potential of the p-n junction, most of $Cu_i(+)$ is pushed away from the depletion region, resulting in higher net acceptor concentrations in the junction area. Figure 5.11 also gives the equilibrium defect distribution the cells under 1 Sun illumination with 0.7V forward bias (or MPP/V_{OC}). In contrast to the dark equilibrium case, under light illumination and forward bias, $Cu_i(+)$ moves deeper into the depletion region due to reduced potential difference across the junction, further decreasing the net acceptor density near the junction. As we have discussed in the experimental section above, expected behavior of Cu dopants is observed for the dark-soaked and forward-biased cell. For the case of dark-soaked and short-circuited device, no significant migration was observed. Based on the evolution of dopant profiles, both our 1D solver and Silvaco Atlas predict an increment in FF for the forward-biased device, as shown in Figure 5.13.

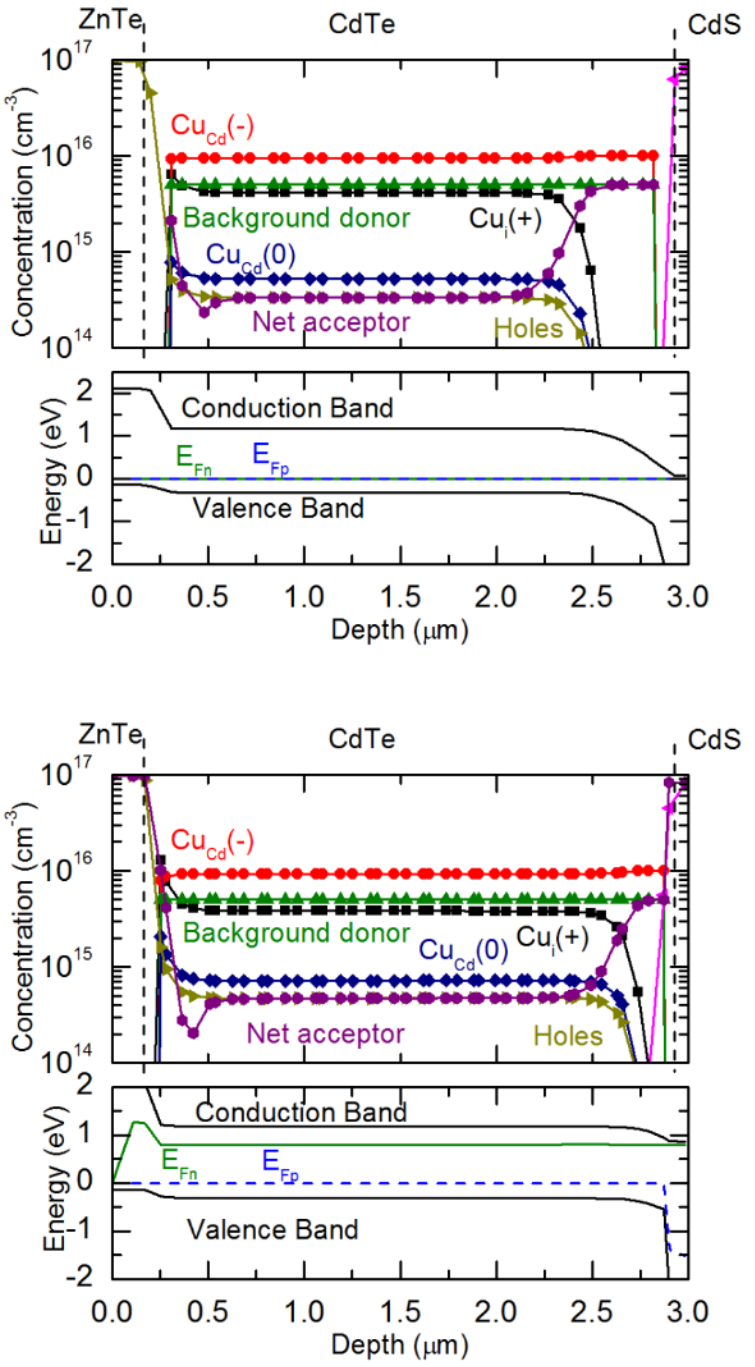

Figure 5.12. Equilibrium of the solar cells under dark condition at 60°C (left) and cells under light soak with forward bias condition at 60°C (right).

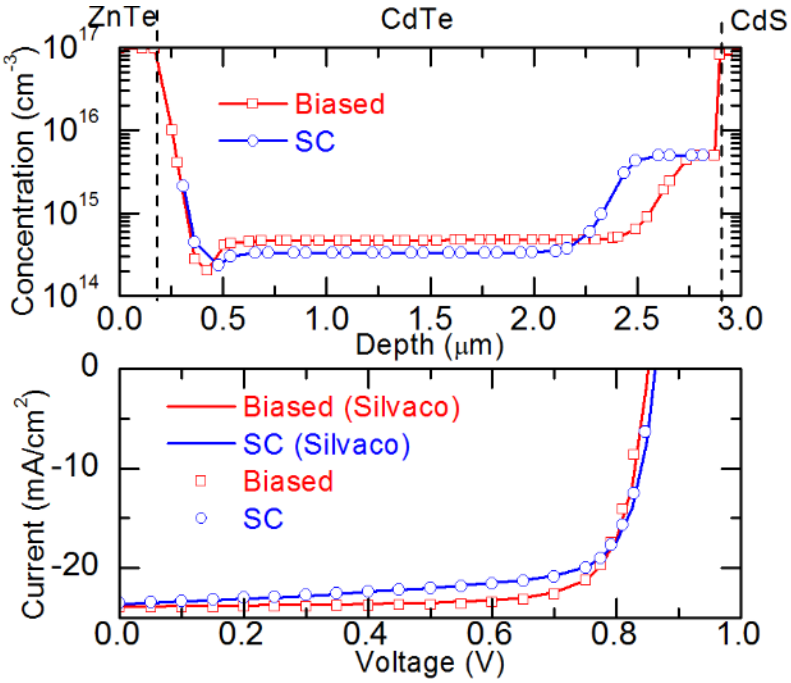

Figure 5.13. Comparison of simulated net acceptor distribution under different bias conditions and their corresponding IV curves.

As a time-dependent solver was employed in this work, continuous migration of the defects and transient behavior of device performance were simulated as well. Simulated device performance changes, under different conditions are presented in Figure 5.14. Again, forward-biased "devices" show performance enhancement while no change is observed in the zero-biased "devices". But, neither does the short-circuit condition decrease FF nor does the forward bias considerably boost V_{OC}. However, both phenomena were presented in our previous work, in which Cu_{Cd}(-) and Cu_i(+) interactions were investigated in the context of long term stability of CdTe solar cells [70]. It is also important to point out that very small diffusion coefficients were applied in simulations in order to achieve hours-long metastability behaviour. Using DFT number results in performance changes completed in less than 0.1 hour.

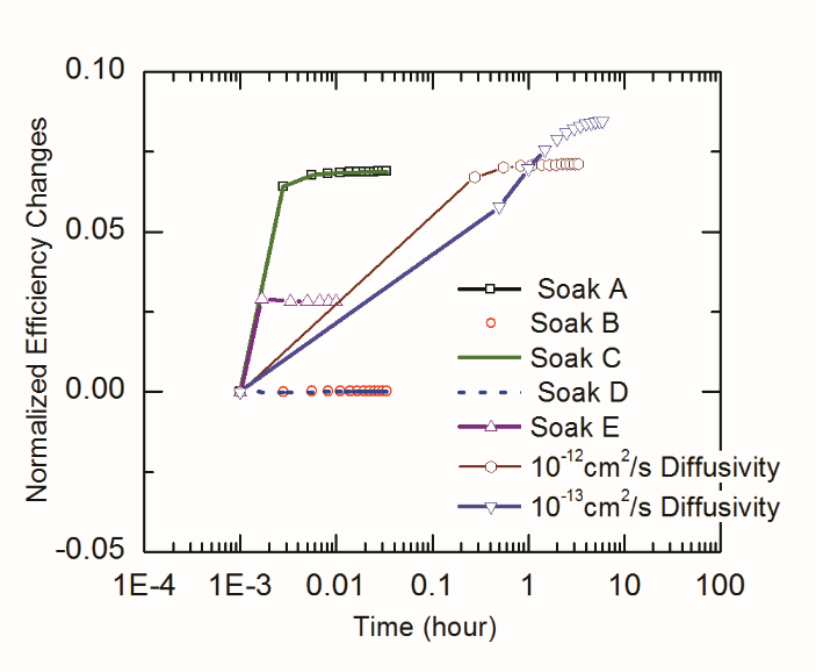

Figure 5.14. Device performance changes as a function of soaking time with various conditions. See Table 5.1 below for the conditions applied for each simulation.

Table 5.1 List of Different Soaking Conditions

Soak	Illumination	Voltage Bias	Mechanism
A	1 Sun	0.8 V	Light & Biased
B	1 Sun	0 V	Light & Short-Circuit
C	Dark	0.8V	Dark & Biased
D	Dark	0 V	Dark & Short-Circuit
E	1 Sun	0.8 V	No Diffusion
F	1 Sun	0.8 V	Small Diffusivity 10^{-12} cm^2/s
G	1 Sun	0.8 V	Small Diffusivity 10^{-13} cm^2/s

Soak F & G are simulated with smaller Cu_i diffusivity.

To address such huge discrepancies among first principle calculation, experiment and simulations, interaction of Cu and Cl in real CdTe absorbers, that lead to formation of

pair complexes, introducing new mechanisms of slow defect migration and new instability mechanisms related to association/dissociation of complexes [27], which were listed in Section 3.3 above, were investigated by the same approach as well. Nanmely, anneal simulations and complete dark soak were performed to provide "device" for following metastability researches.

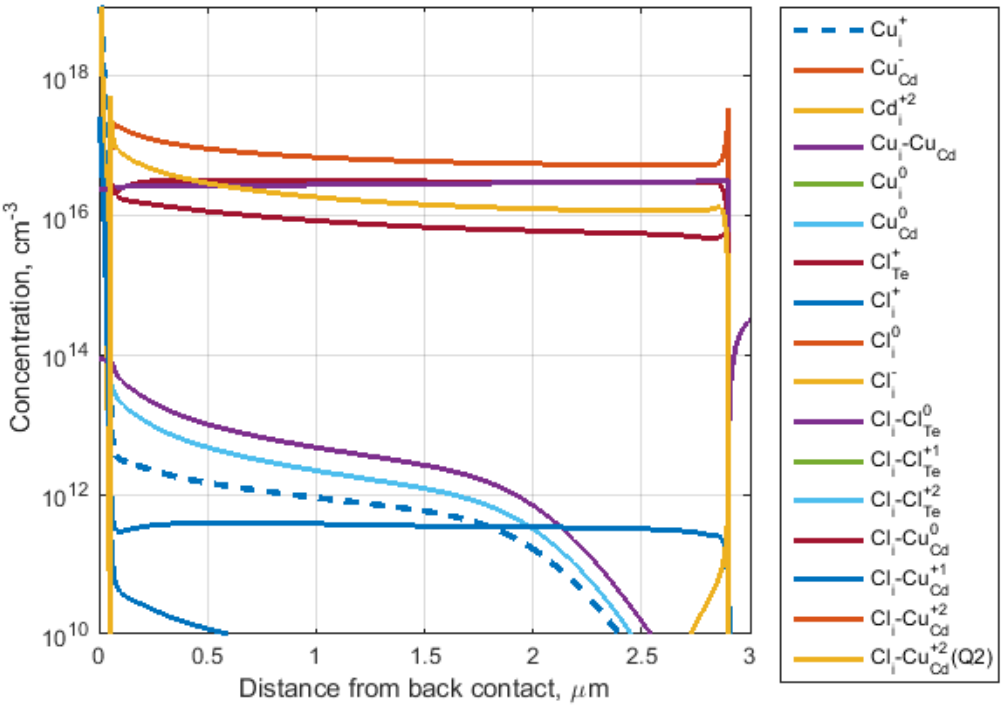

Figure 5.15. Equilibrium of the solar cells under dark condition at 60°C. Blue dash line for $Cu_i(+)$ donor.

Figure 5.15 shows typical point defect profiles achieved with both Cu and Cl point defects in simulations. It is important to note that due to more complicated and compensated defect chemistry, total Cu concentration as high as $10^{17}cm^{-3}$ can be achieved. On the left, defect distribution and net dopant concentration are plotted for the device with

complete dark soak, where stronger non-uniform doping was achieved. In Figure 5.16 below, distributions are plotted after extended light soak under 60°C for 30 hours with forward bias applied. Again, due to the smaller electric field presented in the junction of this case, much more mobile donors migrated towards junction area, thus reduced doping concentration and rasied depletion region width in the CdTe absorber layer. Futher investigation on these defect systems could be conducted to achieve doping profiles that can be somewhat verified by experiments.

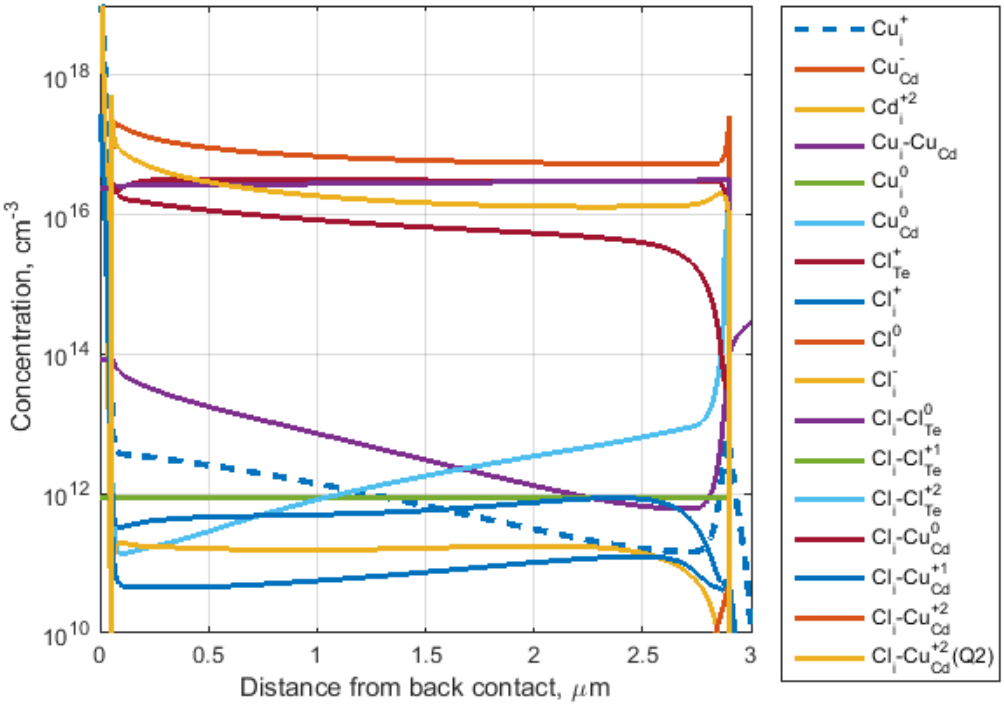

Figure 5.16. Equilibrium of the solar cells under light soak conditions with forward bias at 60°C. Blue dash line for $Cu_i(+)$ donor.

Similarly to the simplified case, these new simulations shows comparable device performance changes induced by defect migration, as shown in Figure 5.16 below. Further

more, due to the complicated defect reactions, complexes associated with mobile dopants more specifically, lower concentration of mobile ions is achived in simulations. Thus, the migration of mobile ions are limited by the dissociation rate of these complexes. Results in significantly reduced rate of device performance changes. Even using first principle calculated defect parameters, 20 hour long metastable behaviour can be achieved in simulation, which can not be done by the previous over simplified case. However, more effort is required to reproduce the excat curves obtained from simulation demonstrated in Figure 5.11.

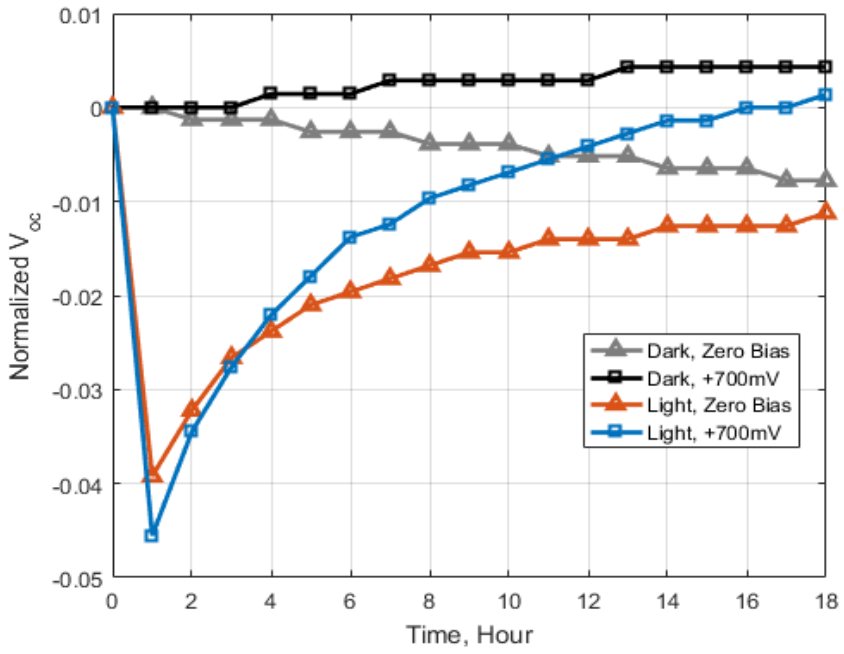

Figure 5.17 Normliazed Voc changes under different light sokaing conditions with first principle calculated diffusion-reaction parameters.

CHAPTER 6

CONCLUSIONS

A self-consistent 1D numerical solver for simulating defect migration in CdTe was successfully implemented with advanced kinetic models, including defect reactions and defect-carrier interactions developed. Time-dependent Drift-Diffusion equations for the mobile atomistic defects are solved using the Schafetter-Gummel discretization scheme, to investigate their migration under the complicated annealing and operating conditions of the solar cells. The reactions of point defects, including defect-defect interactions and defect-free carrier interactions are isolated from the drift-diffusion part and solved by a unique implicit scheme in the time domain to maintain total atom conservation and to avoid unphysical concentration introduction as a numerical artifact of the regular explicit scheme. This approach also enables the usage of larger time intervals in time domains with acceptable accuracy in most cases.

The drift-diffusion model used in semiconductor device simulators has been integrated into the Unified Solver, by a two-loop scheme, to the obtain real-time electronic environment based on the ever-changing profiles of point defects. Potential oscillations introduced by this coupling scheme are significantly reduced by an ad-hoc treatment, in which the practical time domain discretization with less computational burden is assured under different simulation conditions. Inside this device simulator, automatic damping is applied to resolve devastating electronic subsystems with harsh point defect (dopants) profiles that could generate divergent solutions of the electrostatic potentials and have catastrophic effects on the evolution of point defects. The device simulator, also models real-time solar cell performance under different stress and operation conditions.

Furthermore, it enables maximum power point tracking, short-circuit, open-circuit and different voltage-bias conditions of solar cells in the simulations for a variety common stress tests in the field of photovoltaic device reliability. Hence, correlation between point defect evolution and performance changes introduced by these test conditions can be investigated utilizing this scheme.

Good agreement with the atomic concentration profiles of Cu in CdTe was achieved between simulation and experiment on ZnTe:Cu/sx-CdTe samples. Simulation results further suggest a possible explanation for "slow" diffusion of Cu profiles observed in CdTe material: the internal electric field between the Cu-doped p-type region and the Cu-free intrinsic or slightly doped region, creates substantial drift flux of $Cu_i(+)$ mobile ions in the reverse direction of the diffusion flux of the same species, which in general limits the "diffusion" velocity of Cu atoms overall. Simulation results also indicate that the formation of the $Cu_{Cd}(-)$ acceptor itself, consumes the main diffuser, $Cu_i(+)$, and slows down the overall diffusion process as well. This investigation further demonstrates that the Cu solubility is a complicated equilibrium states between different species of point defects. In this simplified model, increasing the source concentration of $Cu_i(+)$ could successfully raise Cu's "solubility" in CdTe material. The speculated reason of the observed Cu dips in the CdTe bulk near the source layer interface, back diffusion of $Cu_i(+)$ during the cool down process, is also confirmed by simulations in this work, with segregation factors applied.

Based on this over-simplified model of the Cu chemistry in CdTe, migration of Cu atoms under different stress conditions were also investigated, both in the long term

reliability field and in the short-term metastability area. Cu depletion during long term SC stress was successfully simulated by this solver, with Fill Factor-induced device performance degradation, that is reported in experimental works. Simulations on the short-term metastability of CdTe solar cells further suggest such recoverable performance changes are partially, if not solely, caused by the drift-diffusion process of point defects, as a result of changing environment and evolving electronic subsystems.

The flexibility and healthiness of the solver developed in this work is further confirmed by more complicated Cu-Cl co-existence models. In these cases, more than 17 point defects and 19 reactions are successfully integrated in this Unified Solver. Simulation of Cu annealing in Cl-treated poly-crystalline CdTe solar cells delivered qualitative matching between experimental and simulated Cu profiles in these devices. Similar agreement in the concentrations of free carriers is also obtained between experiment and simulation. Due to the complicated defect chemistry in these advanced models, in agreement of experimental findings, 20-hour long defect migration and metastable device performance are achieved in simulations, with first principle calculated diffusion parameters of Cu and Cl interstitial defects. These simulations could potentially explain the huge discrepancy between slow device performance changes and fast diffusion parameters of common point defects in CdTe thin-film photovoltaic devices.

REFERENCES

[1] B. E. McCandless and J. R. Sites, “Chapter 14 of Handbook of Photovoltaic Science and Engineering.” West Sussex, UK: John Wiley & Sons, 2011.

[2] I. M. Dharmadasa, “Review of the CdCl2 treatment used in CdS/CdTe thin film solar cell development and new evidence towards improved understanding,” *Coatings*, vol. 4, no. 2, pp. 282–307, 2014.

[3] J. Britt and C. Ferekides, “Thin-film CdS/CdTe solar cell with 15.8% efficiency,” *Appl. Phys. Lett.*, vol. 62, no. 22, p. 2851, May 1993.

[4] F. Solar, “First Solar Achieves Yet Another Cell Conversion Efficiency World Record,” 2016. .

[5] J. N. Duenow *et al.*, “Single-crystal CdTe solar cells with Voc greater than 900 mV,” *Appl. Phys. Lett.*, vol. 105, no. 5, p. 53903, 2014.

[6] M. Gloeckler, I. Sankin, and Z. Zhao, “CdTe solar cells at the threshold to 20% efficiency,” *IEEE J. Photovoltaics*, vol. 3, no. 4, pp. 1389–1393, 2013.

[7] J. Sites and J. Pan, “Strategies to increase CdTe solar-cell voltage,” *Thin Solid Films*, vol. 515, no. 15, pp. 6099–6102, 2007.

[8] J. Perrenoud *et al.*, “A comprehensive picture of Cu doping in CdTe solar cells,” *J. Appl. Phys.*, vol. 114, no. 17, 2013.

[9] A. Moore, T. Fang, and J. Sites, “Cu Profiles in CdTe Solar Cells,” in *Proceedings of the 42th IEEE Photovoltaic Specialist Conference*, 2015.

[10] C. Gretener *et al.*, “New perspective on the performance stability of CdTe solar cells,” *Sol. Energy Mater. Sol. Cells*, vol. 146, pp. 51–57, Mar. 2016.

[11] J. V Li *et al.*, “Electrical characterization of Cu composition effects in CdS/CdTe thin-film solar cells with a ZnTe: Cu back contact,” *IEEE J. Photovoltaics*, vol. 3, no. 3, pp. 1095–1099, 2013.

[12] B. E. McCandless and K. D. Dobson, “Processing options for CdTe thin film solar cells,” *Sol. Energy*, vol. 77, no. 6, pp. 839–856, 2004.

[13] P. R. Kharangarh, D. Misra, G. E. Georgiou, and K. K. Chin, “Characterization of space charge layer deep defects in n+-CdS/p-CdTe solar cells by temperature dependent capacitance spectroscopy,” *J. Appl. Phys.*, vol. 113, no. 14, p. 144504, Apr. 2013.

[14] T. A. Gessert, W. K. Metzger, P. Dippo, S. E. Asher, R. G. Dhere, and M. R. Young, “Dependence of carrier lifetime on Cu-contacting temperature and ZnTe: Cu thickness in CdS/CdTe thin film solar cells,” *Thin Solid Films*, vol. 517, no. 7, pp. 2370–2373, 2009.

[15] D. Kuciauskas *et al.*, “Recombination Analysis in Cadmium Telluride Photovoltaic Solar Cells With Photoluminescence Spectroscopy,” *IEEE Journal of Photovoltaics*, vol. 6, no. 1. pp. 313–318, 2016.

[16] R. Akis *et al.*, “Extracting Cu diffusion parameters in polycrystalline CdTe,” in *Proceedings of the 40th IEEE Photovoltaic Specialist Conference*, 2014.

[17] J. Ma, S.-H. Wei, T. A. Gessert, and K. K. Chin, “Carrier density and compensation in semiconductors with multiple dopants and multiple transition energy levels: Case of Cu impurities in CdTe,” *Phys. Rev. B*, vol. 83, no. 24, p. 245207, 2011.

[18] J. F. Hiltner and J. R. Sites, “Stability of CdTe solar cells at elevated temperatures: bias, temperature, and Cu dependence,” in *National Center for Photovoltaics (NCPV) 15th Program Review Meeting*, 1999, vol. 462, no. 1, pp. 170–175.

[19] D. Brinkman *et al.*, “Self-consistent simulation of CdTe solar cells with active defects,” *J. Appl. Phys.*, vol. 118, no. 3, p. 35704, 2015.

[20] P. Capper, *Properties of narrow gap cadmium-based compounds*, no. 10. Iet, 1994.

[21] S.-H. Wei, S. B. Zhang, and A. Zunger, “First-principles calculation of band offsets, optical bowings, and defects in CdS, CdSe, CdTe, and their alloys,” *J. Appl. Phys.*, vol. 87, no. 3, pp. 1304–1311, 2000.

[22] D. Krasikov, A. Knizhnik, B. Potapkin, and T. Sommerer, "Why shallow defect levels alone do not cause high resistivity in CdTe," *Semicond. Sci. Technol.*, vol. 28, no. 12, 2013.

[23] D. Krasikov, A. Knizhnik, B. Potapkin, S. Selezneva, and T. Sommerer, "First-principles-based analysis of the influence of Cu on CdTe electronic properties," *Thin Solid Films*, vol. 535, pp. 322–325, 2013.

[24] J.-H. Yang, J.-S. Park, J. Kang, W. Metzger, T. Barnes, and S.-H. Wei, "Tuning the Fermi level beyond the equilibrium doping limit through quenching: The case of CdTe," *Phys. Rev. B*, vol. 90, no. 24, p. 245202, 2014.

[25] J. Ma, J. Yang, S.-H. Wei, and J. L. F. Da Silva, "Correlation between the electronic structures and diffusion paths of interstitial defects in semiconductors: The case of CdTe," *Phys. Rev. B*, vol. 90, no. 15, p. 155208, 2014.

[26] J.-H. Yang, J.-S. Park, J. Kang, and S.-H. Wei, "First-principles multiple-barrier diffusion theory: The case study of interstitial diffusion in CdTe," *Phys. Rev. B*, vol. 91, no. 7, p. 75202, 2015.

[27] D. Krasikov and I. Sankin, "Defect interactions and the role of complexes in the CdTe solar cell absorber," *J. Mater. Chem. A*, vol. 5, no. 7, pp. 3503–3513, 2017.

[28] D. Hofmann, P. Omling, H. Grimmeiss, B. Meyer, K. Benz, and D. Sinerius, "Identification of the chlorine A center in CdTe," *Phys. Rev. B*, vol. 45, no. 11, pp. 6247–6250, 1992.

[29] B. G. Mendis, D. Gachet, J. D. Major, and K. Durose, "Long Lifetime Hole Traps at Grain Boundaries in CdTe Thin-Film Photovoltaics," *Phys. Rev. Lett.*, vol. 115, no. 21, p. 218701, Nov. 2015.

[30] D. Kuciauskas *et al.*, "The impact of Cu on recombination in high voltage CdTe solar cells," *Appl. Phys. Lett.*, vol. 107, no. 24, p. 243906, Dec. 2015.

[31] J. A. del Cueto and B. von Roedern, "Long-term transient and metastable effects in cadmium telluride photovoltaic modules," *Prog. Photovoltaics Res. Appl.*, vol. 14, no. 7, pp. 615–628, Nov. 2006.

[32] R. A. Sasala and J. R. Sites, “Time dependent voltage in CuInSe/sub 2/ and CdTe solar cells,” in *Conference Record of the Twenty Third IEEE Photovoltaic Specialists Conference - 1993 (Cat. No.93CH3283-9)*, 1993, pp. 543–548.

[33] T. Sample, “Preconditioning of Thin-Film PV Modules Through Controlled Light-Soaking,” in *NREL Photovoltaic Module Reliability Workshop*, 2012.

[34] M. Propst, K. Goshia, and J. Hevelone, “Effects of Various Module Preconditioning Procedures on CdTe Pmax Measurements,” in *NREL PV Module Reliability Workshop 2010*, 2010.

[35] B. R. Tetali, “Stability studies of CdTe/CdS thin film solar cells,” University of South Florida, 2005.

[36] S. Demtsu, “Impact of back-contact materials on performance and stability of CdS/CdTe solar cells,” Colorado State University, 2006.

[37] C. R. Corwine, A. O. Pudov, M. Gloeckler, S. H. Demtsu, and J. R. Sites, “Copper inclusion and migration from the back contact in CdTe solar cells,” *Sol. Energy Mater. Sol. Cells*, vol. 82, no. 4, pp. 481–489, 2004.

[38] E. D. Jones, N. M. Stewart, and J. B. Mullin, “The diffusion of copper in cadmium telluride,” *J. Cryst. Growth*, vol. 117, no. 1, pp. 244–248, 1992.

[39] G. Teeter and S. Asher, “Modeling Cu migration in CdTe solar cells under device-processing and long-term stability conditions,” in *2008 33rd IEEE Photovolatic Specialists Conference*, 2008, pp. 1–6.

[40] D. Mao, G. Blatz, C. E. Wickersham, and M. Gloeckler, “Correlative impurity distribution analysis in cadmium telluride (CdTe) thin-film solar cells by ToF-SIMS 2D imaging,” *Sol. Energy Mater. Sol. Cells*, vol. 157, pp. 65–73, 2016.

[41] H. Wolf, F. Wagner, and T. Wichert, “Anomalous diffusion profiles of Ag in CdTe due to chemical self-diffusion.,” *Phys. Rev. Lett.*, vol. 94, no. 12, p. 125901, Apr. 2005.

[42] H. Wolf, F. Wagner, T. Wichert, R. Grill, E. Belas, and I. Collaboration, “Internal drift effects on the diffusion of Ag in CdTe,” *J. Electron. Mater.*, vol. 35, no. 6, pp.

1350–1353, 2006.

[43] P. M. Fahey, P. B. Griffin, and J. D. Plummer, “Point defects and dopant diffusion in silicon,” *Rev. Mod. Phys.*, vol. 61, no. 2, pp. 289–384, 1989.

[44] S. M. Hu, “Nonequilibrium point defects and diffusion in silicon,” *Mater. Sci. Eng. R Reports*, vol. 13, no. 3, pp. 105–192, 1994.

[45] S.-H. Wei and S. B. Zhang, “Chemical trends of defect formation and doping limit in II-VI semiconductors: The case of CdTe,” *Phys. Rev. B*, vol. 66, no. 15, p. 155211, 2002.

[46] D. L. Scharfetter and H. Gummel, “Large-signal analysis of a silicon read diode oscillator,” *IEEE Trans. Electron Devices*, vol. 16, no. 1, pp. 64–77, 1969.

[47] D. Guo *et al.*, “Numerical Simulation of Copper Migration in Single Crystal CdTe,” *IEEE J. Photovoltaics*, vol. 6, no. 5, pp. 1286–1291, Sep. 2016.

[48] M. S. Lundstrom and R. J. Schuelke, “Numerical analysis of heterostructure semiconductor devices,” *IEEE Trans. Electron Devices*, vol. 30, no. 9, pp. 1151–1159, 1983.

[49] K. Tomizawa, *Numerical simulation of submicron semiconductor devices*. Artech House, 1993.

[50] D. Vasileska, S. M. Goodnick, and G. Klimeck, *Computational Electronics: Semiclassical and Quantum Device Modeling and Simulation*. CRC press, 2016.

[51] J. Li *et al.*, “Controlled activation of ZnTe: Cu contacted CdTe solar cells using rapid thermal processing,” *Sol. Energy Mater. Sol. Cells*, vol. 133, pp. 208–215, 2015.

[52] C. A. Wolden *et al.*, “The roles of ZnTe buffer layers on CdTe solar cell performance,” *Sol. Energy Mater. Sol. Cells*, vol. 147, pp. 203–210, Apr. 2016.

[53] H. C. Chou, A. Rohatgi, N. M. Jokerst, E. W. Thomas, and S. Kamra, “Copper migration in CdTe heterojunction solar cells,” *J. Electron. Mater.*, vol. 25, no. 7,

pp. 1093–1098, 1996.

[54] M. Tuteja, P. Koirala, S. MacLaren, R. Collins, and A. Rockett, “Direct observation of electrical properties of grain boundaries in sputter-deposited CdTe using scan-probe microwave reflectivity based capacitance measurements,” *Appl. Phys. Lett.*, vol. 107, no. 14, p. 142106, Oct. 2015.

[55] W. Xia *et al.*, “Te/Cu bi-layer: A low-resistance back contact buffer for thin film CdS/CdTe solar cells,” *Sol. Energy Mater. Sol. Cells*, vol. 128, pp. 411–420, 2014.

[56] Y. G. Fedorenko, J. D. Major, A. Pressman, L. J. Phillips, and K. Durose, “Modification of electron states in CdTe absorber due to a buffer layer in CdTe/CdS solar cells,” *J. Appl. Phys.*, vol. 118, no. 16, p. 165705, Oct. 2015.

[57] K. D. Dobson, I. Visoly-Fisher, G. Hodes, and D. Cahen, “Stability of CdTe/CdS thin-film solar cells,” *Sol. Energy Mater. Sol. Cells*, vol. 62, no. 3, pp. 295–325, 2000.

[58] C. Gretener *et al.*, “New perspective on the performance stability of CdTe solar cells,” *Sol. Energy Mater. Sol. Cells*, vol. 146, pp. 51–57, Mar. 2016.

[59] I. Visoly-Fisher, K. D. Dobson, J. Nair, E. Bezalel, G. Hodes, and D. Cahen, “Factors affecting the stability of CdTe/CdS solar cells deduced from stress tests at elevated temperature,” *Adv. Funct. Mater.*, vol. 13, no. 4, pp. 289–299, 2003.

[60] N. Strevel, L. Trippel, C. Kotarba, and I. Khan, “Improvements in CdTe module reliability and long-term degradation through advances in construction and device innovation,” *Photovoltaics Int.*, vol. 22, 2013.

[61] “Why perovskite solar cells with high efficiency show small IV-curve hysteresis,” *Sol. Energy Mater. Sol. Cells*, vol. 169, pp. 159–166, Sep. 2017.

[62] D. Guo and E. Al., “in preparation.”

[63] D. Kuciauskas, A. Kanevce, P. Dippo, S. Seyedmohammadi, and R. Malik, “Minority-Carrier Lifetime and Surface Recombination Velocity in Single-Crystal CdTe,” *Photovoltaics, IEEE J.*, vol. 5, no. 1, pp. 366–371, 2015.

[64] D. Mao, C. E. Wickersham, and M. Gloeckler, “Measurement of Chlorine Concentrations at CdTe Grain Boundaries,” *IEEE J. Photovoltaics*, vol. 4, no. 6, pp. 1655–1658, 2014.

[65] R. Akis, D. Brinkman, D. Guo, D. Vasileska, and C. Ringhofer, “Simulating Cl diffusion in polycrystalline CdTe,” in *Photovoltaic Specialist Conference (PVSC), 2015 IEEE 42nd*, 2015, pp. 1–4.

[66] Hasitha Mahabaduge, “private communication,” 2015.

[67] A. Moore and J. Sites, “Stability of CdTe solar cells with various back contact methods,” in *2016 IEEE 43rd Photovoltaic Specialists Conference (PVSC)*, 2016, pp. 2218–2222.

[68] S. Demtsu, S. Bansal, and D. Albin, “Intrinsic stability of thin-film CdS/CdTe modules,” in *2010 35th IEEE Photovoltaic Specialists Conference*, 2010, pp. 001161–001165.

[69] A. Moore and J. Sites, “Cu profiles in CdTe solar cells,” in *2015 IEEE 42nd Photovoltaic Specialist Conference (PVSC)*, 2015, pp. 1–5.

[70] D. Guo *et al.*, “Cu Migration and its Impact on the Metastable Behavior of CdTe Solar Cells,” in *Proceedings of the 42th IEEE Photovoltaic Specialists Conference*, 2015.